

Influence of a Counteranion on the Zero-Field Splitting of Tetrahedral Cobalt(II) Thiourea Complexes

Shalini Tripathi,^{†,‡} Shefali Vaidya,^{†,‡} Kamal Uddin Ansari,[†] Naushad Ahmed,[†] Eric Rivière,[§] Lena Spillecke,[⊥] Changhyun Koo,[⊥] Rüdiger Klingeler,^{⊥,||} Talal Mallah,^{*,§,Ⓜ} Gopalan Rajaraman,^{*,†,Ⓜ} and Maheswaran Shanmugam^{*,†,Ⓜ}

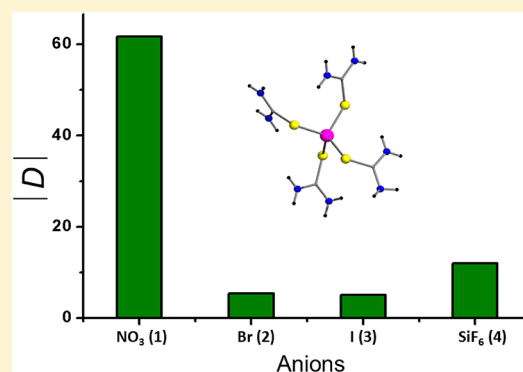
[†]Department of Chemistry, Indian Institute of Technology Bombay, Powai, Mumbai, India

[⊥]Kirchhoff Institute for Physics and ^{||}Centre for Advanced Materials, Heidelberg University, 69120 Heidelberg, Germany

[§]Institut de Chimie Moléculaire et des Matériaux d'Orsay, CNRS, Université Paris Sud, Université Paris Saclay, 91405 Orsay Cedex, France

Supporting Information

ABSTRACT: Four mononuclear cobalt(II) complexes with pseudo tetrahedral geometry were isolated with different counteranions; their structure solution reveals the molecular formula as $[\text{Co}(\text{L}_1)_4]\text{X}_2$ [where $\text{L}_1 = \text{thiourea} (\text{NH}_2\text{CSNH}_2)$ and $\text{X} = \text{NO}_3$ (1), Br (2), and I (3)] and $[\text{Co}(\text{L}_1)_4](\text{SiF}_6)$ (4). The detailed analysis of direct-current (dc) magnetic data reveals a zero-field splitting (ZFS; D) with $m_s = \pm 3/2$ as the ground levels ($D < 0$) for the four complexes. The magnitude of the ZFS parameter is larger, in absolute value, for 1 ($D = -61.7 \text{ cm}^{-1}$) than the other three complexes (-5.4 , -5.1 , and -12.2 cm^{-1} for 2–4, respectively). The sign of D for 1, 2, and 4 was unambiguously determined by X-band electron paramagnetic resonance (EPR) spectroscopy of the diluted samples (10%) at 5 K. For 3, the sign of D was naturally endorsed from the frequency-dependent out-of-phase signal (χ_M'') observed in the absence of an external dc magnetic field and confirmed by high-frequency EPR (70–600 GHz) experiments performed on a representative pure polycrystalline 3, which gave a quantitative D value of $-5.10(7) \text{ cm}^{-1}$. Further, the drastic changes in the spin Hamiltonian parameters and their related relaxation dynamics phenomena (of 2–4 compared to 1) were rationalized using ab initio complete-active-space self-consistent field/ n -electron valence perturbation theory calculations. Calculations disclose that the anion-induced structural distortion observed in 2–4 leads to a nonfavorable overlap between the π orbital of cobalt(II) and the π^* orbital of the sulfur atom that reduces the overall $|D|$ value in these complexes compared to 1. The present study demonstrates that not only the first but also the second coordination sphere significantly influences the magnitude of the ZFS parameters. Particularly, a reduction of D of up to $\sim 90\%$ occurs (in 2–4 compared to 1) upon a simple variation of the counteranions and offers a viable approach to modulate ZFS in transition-metal-containing single-molecule magnets.



INTRODUCTION

Discrete transition-metal complexes exhibiting slow relaxation of magnetization are classified as single-molecule magnets or single-ion magnets (SMMs or SIMs).^{1–3} When zero-field splitting (ZFS or D) leads to the situation where the $m_s = \pm S$ levels have the lowest energy (negative D value), a barrier for the reorientation of the magnetization [$U_{\text{eff}} = |D|S^2$ for an integer spin system and $|D|(S^2 - 1/4)$ for a noninteger spin] leads to a blocking of the magnetization and thus the occurrence of SMM behavior.^{4–8} One of the objectives in this area of research is to investigate the factors that control not only the nature (positive D or negative D) but also the magnitude of ZFS responsible for the SMM behavior. Understanding this phenomenon is relatively easier for mononuclear metal complexes than for polynuclear ones. For large metal clusters, the magnitude of the axial ZFS parameter

(D) was found to be inversely proportional to S^2 ,^{9–16} which precludes obtaining large $|D|$ values and thus large ZFS energy barriers for molecules possessing very large spin ground states. Mononuclear complexes offer the possibility of designing SMMs with relatively large ZFS, and, more importantly, they allow one, thanks to theoretical calculations, to gain deep insights into the structural parameters that control ZFS. Particularly, cobalt(II)-containing complexes were thoroughly investigated because of the Kramers nature of the spin state, which is expected to block magnetization via the Orbach process when other relaxation mechanisms are absent.^{17–21} Apart from the cobalt(II) ion, there are several promising low-coordinate iron, nickel, and cobalt complexes reported by

Received: March 4, 2019

Published: June 27, 2019

Long, Murugesu, and Gao and co-workers.^{15,22–25} These complexes are found to exhibit strong axial ZFS parameters because of the low coordination number of the metal ions.^{22–24,26} Apart from the low-coordination approach, there are several factors that may be used to control the magnitude and sign of ZFS. Halides allow tuning of the sign and magnitude of D , as was elegantly shown by Long and co-workers in some chromium(III) complexes,²⁷ and a similar effect was probed by Boča and co-workers on several cobalt(II) tetrahedral complexes.^{28,29} Murugesu and co-workers have pointed out the importance of out-of-state spin–orbit coupling in deciding the sign and magnitude of D in some cobalt(II) complexes.³⁰ Peripheral substitution of the coordinating ligand also influences the ZFS of $[\text{Co}^{\text{II}}\text{Co}_3^{\text{III}}]$ complexes reported by Gao and co-workers.³¹ Further, the influence of structural distortion on the D value of certain cobalt(II) tetrahedral complexes decorated by N_2O_2 ligands was investigated by Plass and co-workers.³² The importance of Lewis basicity of an axial ligand to stabilize an easy axis of magnetization (negative D) in a five-coordinate cobalt(II) complexes was reported elsewhere by Sarkar and co-workers and Mallah and co-workers independently.^{15,33–36} More recently, Long and co-workers, some of us, and others proposed that, by exploiting the covalency of the ligated atom to the metal center, the D value can be significantly altered in cobalt(II) tetrahedral complexes.^{23,37–43} Long and co-workers and some of us reported recently the non-negligible influence of the second coordination sphere of tetrahedral cobalt(II) complexes in regulating the D value.^{37,42,43}

Almost all of the above-mentioned factors mainly focus on the effect of the first coordination sphere on the nature and magnitude of ZFS. The study related to the secondary effect due to the cations and/or anions in the crystal lattice, which, in turn, can be correlated to ZFS parameter, is rare in the literature.^{31,44,45} Here we aim at investigating the influence of anions present in the crystal lattice and how they alter the coordination environment around cobalt(II) centers/ZFS. We report a family of complexes with various counteranions, which are structurally characterized by single-crystal X-ray diffraction (XRD). The isolated complexes possess the molecular formulas of $[\text{Co}(\text{L}_1)_4]\text{X}_2$ [where $\text{L}_1 =$ thiourea and $\text{X} = \text{NO}_3$ (1), Br (2), and I (3)] and $[\text{Co}(\text{L}_1)_4](\text{SiF}_6)$ (4). These complexes are found to show different axial ZFS parameters, as confirmed by magnetic studies, which are correlated to the nature of anions in the crystal lattice and rationalized by wavefunction-based calculations.

EXPERIMENTAL SECTION

Unless otherwise stated, all of the reactions were carried out under aerobic conditions. All of the chemicals were purchased from commercially available sources (Alfa Aesar and Sigma-Aldrich) and used without further purification. Magnetic data for the complexes were collected on a MPMS-XL SQUID magnetometer equipped with a 70 kOe superconducting magnet in the temperature range of 300–2 K. The single-crystal X-ray data collection was done on a Rigaku Saturn CCD diffractometer using a graphite monochromator ($\lambda = 0.71073 \text{ \AA}$). The unit cell determination and data reduction were performed using *CrysAlisPro 1.171.38.43* (Rigaku OD, 2015). The structures were solved by direct methods and refined by least-squares procedures on F^2 with *SHELXL-2014/7* (Sheldrick, 2014). All non-hydrogen atoms were refined anisotropically, and hydrogen atoms were added to their geometrically calculated positions and refined as a riding model (CCDC 1878570–1878572). The Fourier transform infrared (FTIR) data were collected on solid samples using KBr pellets

on a PerkinElmer FTIR spectrometer in the 400–4000 cm^{-1} range. Solid-state magic-angle-spinning ^{31}P NMR (^{31}P -MAS NMR) spectra were recorded on a Bruker 750 MHz spectrophotometer with a spinning rate of 10 kHz. High-frequency electron paramagnetic resonance (HF-EPR) measurements were carried out by means of a millimeter vector network analyzer by ABmm, which is used as a microwave source and detector.⁴⁶ The spectra have been taken at various microwave frequencies between 70 and 600 GHz, which were achieved by means of assembling several band diodes, such as V, W, and D bands, etc. A superconducting magnet by Oxford Instruments provides high magnetic fields up to 16/18 T. The temperature is controlled by means of a variable-temperature insert with a helium⁴ gas flow. Powder samples are placed inside a brass sample holder at the end of a transmission-type tube-based probe. No glue or grease has been used so that the loose powder sample is expected to be aligned in the high magnetic field of the experiment.⁴⁷ Evidence of powder alignment is indeed observed because abrupt steps of the initial HF-EPR spectra taken preliminarily to the data presented at hand as well as at low fields. The HF-EPR data are, hence, restricted to $B \geq 1 \text{ T}$.

Computational Details. The quantum-chemical calculations were carried out using the ORCA (4.1.0)⁴⁸ suite directly on the crystal structures obtained through single-crystal XRD. Spin Hamiltonian (SH) parameters were calculated using multireference ab initio calculations. State-average complete-active-space self-consistent-field (CASSCF) calculations were performed on complexes 2–4. Scalar relativistic effects are treated using the ZORA method.^{49,50} The Ahlrichs polarized triple- ζ (TZVP) quality basis set along with TZVP/J as an auxiliary basis set for the resolution of identity approximation for cobalt, sulfur, iodine, phosphorus, and bromine was used, whereas the split-valence plus polarization (SVP) quality basis set along with SVP/J as an auxiliary basis set was used for the rest of the atoms.^{51,52} The calculations were performed with an active space of CAS (7,5), which corresponds to seven active d electrons in five active d orbitals. Here the D and E values are estimated using an effective Hamiltonian approach developed.^{53,54}

Additionally, calculations are also performed using the MOLCAS suite to assess and understand how the estimates of D and E vary. Here calculations were performed on the X-ray structures of all of the complexes with and without counteranions. The basis sets describing all atoms were taken from ANO-RCC library available in the MOLCAS suite. The CASSCF step was performed by considering the 7 active electrons spanning in five 3d orbitals, for the 10 quartets and 40 doublet excited roots under configuration integration to obtain the energy of the spin-free states. All of the computed roots were further mixed by the spin–orbit coupling within the restricted-active-space state interaction (RASSI-SO) step to obtain the energies of the spin–orbit states for cobalt(II) ions for each of the complexes. The obtained spin–orbit multiplets and ab initio computed matrix element of the angular momentum were used by the *SINGLE_ANISO* module to compute the g and D values and local magnetic properties of the metal center.

The detailed synthetic procedure for complexes 2–4 and their zinc analogues are described below. The synthetic procedures for $[\text{Co}(\text{L}_1)_4](\text{NO}_3)_2$ (1) and its diamagnetic analogue (1-Zn) are reported by us elsewhere.³⁷

Synthesis of the Complex $[\text{Co}(\text{L}_1)_4](\text{Br})_2$ (2). A solid thiourea ligand (L_1 ; 1.0 g, 13.1 mmol) was dissolved in warm ethyl acetate (35–40 °C). A cobalt bromide salt (0.717 g, 3.3 mmol) was then added, and the reaction mixture was refluxed for 48 h. After 2 days, the solution was allowed to cool to room temperature and the solvent was removed under vacuum. The obtained residue was dissolved again in ethyl acetate and filtered. The filtrate was kept for crystallization at room temperature without any disturbance. Blue needle-shaped single crystals grew from the filtrate after 1 day; they were suitable for single-crystal XRD. Yield: 0.57 g (34%). IR (KBr, cm^{-1}): 3376 and 3286 (ν_{NH_2}), 1624 ($\nu_{\text{C=S}}$). Calcd: C, 9.18; H, 3.08; N, 21.42; S, 24.51. Found: C, 9.51; H, 3.05; N, 20.95; S, 23.96.

Synthesis of the Complex [Co(L₁)₄](I)₂ (3). A synthetic procedure similar to that of 2 was followed to isolate 3 but, in place of CoBr₂, CoI₂ (1.02 g, 3.3 mmol) was used. The single crystals obtained from ethyl acetate were not suitable for single-crystal XRD, while the crystallization using ethanol yielded suitable single crystals of 3. Yield: 0.62 g (31%). IR (KBr, cm⁻¹): 3375 and 3321 (ν_{NH₂}), 1619 (ν_{C=S}). Calcd: C, 7.78; H, 2.61; N, 18.15; S, 20.78. Found: C, 7.87; H, 2.58; N, 18.55; S, 20.60.

Synthesis of the Complex [Co(L₁)₄](SiF₆) (4). To the warm (35–40 °C) 1-butanol solution of Co(NO₃)₂·6H₂O (0.96 g, 3.3 mmol) was added 4 equiv of L₁ (1.0 g, 13.1 mmol). The reaction mixture was stirred for 5 min, and NH₄PF₆ (1.07 g, 6.6 mmol) was added. The resultant reaction mixture was heated under reflux for 3 h, then cooled to room temperature, filtered, and kept for crystallization. Blue block-shaped crystals suitable for single-crystal XRD were obtained after 2 days upon slow evaporation of the filtrate. Yield: 0.253 g (15%). IR (KBr, cm⁻¹): 3425 and 3400 (ν_{NH₂}), 1616 (ν_{C=S}). Calcd: C, 9.50; H, 3.19; N, 22.17; S, 25.37. Found: C, 9.71; H, 3.2; N, 22.56; S, 24.92.

Note: We have not added any silicon precursor to the reaction; presumably this must have originated from the borosilicate round-bottom flask/crystallization vial utilized.

Synthesis of the Complex [Zn(L₁)₄](Br)₂ (2-Zn). The same synthetic procedure as that for 2 was followed, but CoBr₂ was replaced by ZnBr₂ (0.74 g, 3.3 mmol). White needle-shaped crystals suitable for single-crystal XRD were grown from ethyl acetate after 1 day. Yield: 0.483 g (27.7%). IR (KBr, cm⁻¹): 3384 and 3317 (ν_{NH₂}), 1631 (ν_{C=S}). Calcd: C, 9.07; H, 3.04; N, 21.15; S, 24.21. Found: C, 9.15; H, 2.88; N, 21.58; S, 23.98.

Synthesis of the Complex [Zn(L₁)₄](I)₂ (3-Zn). The same synthetic procedure as that for 3 was followed, but ZnI₂ (1.05 g, 3.3 mmol) was employed instead of CoI₂. Colorless block-shaped crystals suitable for single-crystal XRD were grown from ethanol after 1 day. Yield: 0.332 g (16%). IR (KBr, cm⁻¹): 3392 and 3320 (ν_{NH₂}), 1640 (ν_{C=S}). Calcd: C, 7.70; H, 2.59; N, 17.97%; S, 20.57. Found: C, 8.05; H, 2.32; N, 17.52; S, 20.43.

Synthesis of the Complex [Zn(L₁)₄](SiF₆) (4-Zn). The same synthetic procedure as that for complex 4 was followed, but in place of Co(NO₃)₂·6H₂O, Zn(NO₃)₂·6H₂O (0.978 g, 3.3 mmol) was used. Colorless block-shaped crystals suitable for single-crystal XRD were obtained after 2 days upon slow evaporation from the filtrate. Yield: 0.194 g (11.5%). IR (KBr, cm⁻¹): 3387 and 3324 (ν_{NH₂}), 1632 (ν_{C=S}). Calcd: C, 9.38; H, 3.15; N, 21.89; S, 25.05. Found: C, 9.01; H, 2.93; N, 21.98; S, 24.63.

Note: The unit cell of 4-Zn exactly matches that of its parent complex 4. Therefore, 4-Zn is expected to have (SiF₆)²⁻ as a counteranion in the crystal lattice like 4, which is presumably originated from the borosilicate round-bottom flask/crystallization vial utilized for the reaction/crystallization.

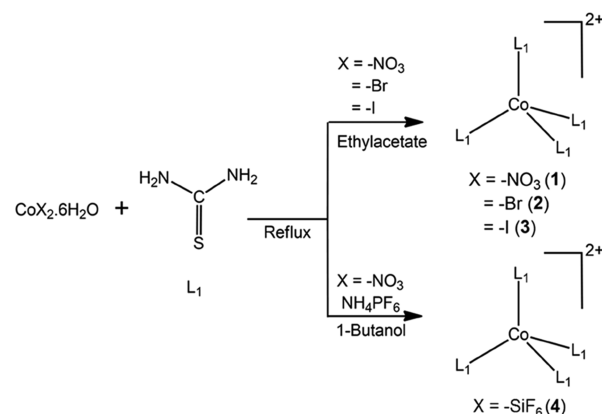
Synthesis of 10% Diluted Samples of 2 and 4. We used the same synthetic procedure as that for the pure compounds but using the corresponding cobalt(II) and zinc(II) salts with a molar ratio of Co:Zn = 1:9. The crystals of the diluted compounds had the same but lighter color than those of the pure ones.

Note: The unit cell of complexes 2-Zn and 4-Zn were checked, and the unit cell parameters are similar to those of their parent paramagnetic analogues 2 and 4, confirming that the 2-Zn–4-Zn complexes possess similar structure and packing arrangement within the crystal lattice. The phase purities of complexes 2–4 and their zinc analogues (2-Zn and 4-Zn) were checked by powder X-ray diffraction (PXRD). The experimental PXRD data of 2-Zn and 4-Zn are in good agreement with the simulated data derived from their corresponding paramagnetic single-crystal data (Figures S1 and S2). Although the 3-Zn unit cell matches the unit cell of 3, attempts to synthesize 10% dilution samples failed because 3 and 3-Zn crystallized separately in the same vial.

RESULT AND DISCUSSION

A series of tetrahedral complexes were obtained upon refluxing of the cobalt salts with various anions in the presence of thiourea in ethyl acetate/alcoholic solution (Scheme 1).

Scheme 1. General Synthetic Procedure Followed To Isolate Complexes 1–4



All of the complexes were isolated as single crystals, and their three-dimensional structures were determined by single-crystal XRD. The detailed synthetic procedure and magnetic studies for complex 1 were reported elsewhere,³⁷ but we have recalled some of its data here for a comparison with the other structurally related complexes (2–4).

Complexes 2 and 3 crystallize in the monoclinic, *P*₂₁/*c* space group, while 4 crystallizes in the orthorhombic, *Pbca* space group (Table 1). In all of the complexes (2–4), the asymmetric unit contains the entire molecule with its corresponding anions in the unit cell. This is in contrast

Table 1. Crystallographic Parameters for Complexes 2–4

	2	3	4
formula	C ₄ H ₁₆ Br ₂ CoN ₈ S ₄	C ₄ H ₁₆ CoI ₂ N ₈ S ₄	C ₄ H ₁₆ CoF ₆ N ₈ SiS ₄
size [mm]	0.26 × 0.09 × 0.02	0.25 × 0.21 × 0.2	0.25 × 0.21 × 0.16
system	monoclinic	monoclinic	orthorhombic
space group	<i>P</i> ₂ ₁ / <i>c</i>	<i>P</i> ₂ ₁ / <i>c</i>	<i>Pbca</i>
<i>a</i> [Å]	17.1546(4)	18.0217(4)	17.4180(10)
<i>b</i> [Å]	9.8267(2)	9.9167(2)	9.6011(4)
<i>c</i> [Å]	10.7390(2)	10.9730(3)	22.2157(10)
α [deg]	90.0	90.0	90.0
β [deg]	91.173(2)	91.773(2)	90.0
γ [deg]	90.0	90.0	90.0
<i>V</i> [Å ³]	1809.93(7)	1960.11(8)	3715.2(3)
<i>Z</i>	4	4	8
ρ _{calcd} [g cm ⁻³]	1.920	2.092	1.818
2θ _{max}	49.9	50.48	49.9
radiation	Mo Kα	Mo Kα	Mo Kα
λ [Å]	0.71073	0.71073	0.71073
<i>T</i> [K]	150(2)	150(2)	150(2)
no. of reflns	17708	7118	16662
no. of indep reflns	3190	3718	3275
reflns with <i>I</i> > 2σ(<i>I</i>)	2935	3526	2597
R1	0.0316	0.0206	0.0506
wR2	0.0858	0.0622	0.1115

with the number of molecules present in the asymmetric unit of the parent complex **1**, where two crystallographically distinct molecules (labeled **1a** and **1b**) are present in the unit cell.

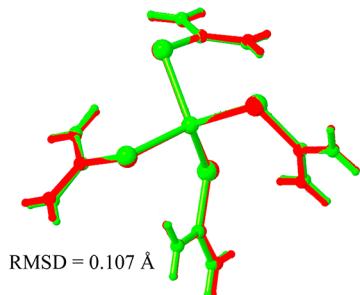
In all of the complexes (**1–4**), each divalent cobalt ion is surrounded by four neutral thiourea (L_1) ligands, which leaves an overall divalent positive charge for the molecular species. This divalent cationic charge is neutralized by two nitrates (in **1**), two bromides (in **2**), two iodides (in **3**), and one hexafluorosilicate (in **4**). We would like to point out here that, for the isolation of **4**, we have not employed any silicon precursor, which presumably originates from the borosilicate glassware employed for the reaction/crystallization. The average Si–F bond distance [1.681(3) Å] observed in **4** is consistent with the bond distance reported for the other metal complexes containing a $(\text{SiF}_6)^{2-}$ anion [average Si–F bond distance = 1.680(6) Å].^{55,56} Because **4** consists of only one anion in the crystal lattice, on the basis of the charge-balance requirement and the average bond distance observed for P–F [1.53–1.58(4) Å]^{57–59} being significantly shorter than the average Si–F bond distance observed in **4**, one can safely neglect the possibility of the presence of a $-\text{PF}_6$ anion in the crystal lattice of **4**. The solid-state ^{31}P -MAS NMR spectrum recorded for **4** with a spinning rate of 10 kHz does not show any NMR signal corresponding to phosphorus, which further validates our observation (Figure S3).

In all of the complexes, the cobalt(II) coordination sphere has a distorted tetrahedral geometry. The extent of deviation from ideal tetrahedral geometry observed in the parent complex **1** is significant compared to that of the other complexes (**2–4**), which is confirmed by the continuous shape measurement (CShM) analysis (Figure S4 and Table S1) value.⁶⁰ In general, the CShM value of zero represents an ideal tetrahedral geometry around the cobalt(II) ion, while a nonzero CShM value relates to the extent of distortion observed from the ideal geometry around the metal ion.

The cobalt(II) ion in complexes **2–4** possesses a geometry close to the ideal tetrahedral geometry (with respect to the first coordination sphere; CShM values of 0.28, 0.22, and 0.09 respectively for **2–4**), while for **1**, the geometry is rather distorted (CShM value of 3.08). The average Co–S bond lengths are found to be equal to 2.3116(13) Å (**1**), 2.3171(10) Å (**2**), 2.3193(8) Å (**3**), and 2.2975(14) Å (**4**), and the average bond angles $\angle\text{S–Co1–S}$ in complexes **1–4** are observed to be 110.03(5)° (**1**), 109.25(4)° (**2**), 109.29(3)° (**3**), and 109.44(5)° (**4**) (see Table 2 for selected bond lengths and bond angles for all of the complexes). All of the complexes are structurally analogous to each other, and their crystal structures are shown in Figure 1.

In particular, complexes **2** and **3** are structural isomorphs of each other, which is evident from the crystallographic and structural parameters of **2** and **3**. To prove the structural resemblance between **2** and **3**, the metal complexes were overlaid on top of each other, and the resultant root-mean-square standard deviation (RMSD) for the entire molecule was calculated, which is observed to be 0.107 Å. Consistent with this observation, very slight changes are noticed in the bond length and bond angle parameters of complexes **2** and **3** (Table 2). As was well established earlier by us³⁷ and Neese and co-workers,⁴³ θ and ω (refer to Figure 11A for details) are the two predominant factors that control not only the magnitude of D but also its sign. Because not much deviation is observed in both the θ and ω parameters for **2** and **3**, conceivably the

Table 2. Selected Bond Lengths and Bond Angles for Complexes **2–4**^a



label	2	3	Δ	4
Bond Length/Å				
Co1–S11	2.3217(10)	2.3104(8)	0.0113	2.2835(15)
Co1–S21	2.3250(10)	2.3255(8)	0.0005	2.2970(13)
Co1–S31	2.3423(10)	2.3392(8)	0.0031	2.2995(14)
Co1–S41	2.2772(11)	2.3021(8)	0.0249	2.3099(13)
Bond Angle/deg				
S11–Co1–S21	103.80(4)	104.55(3)	0.75	109.33(6)
S11–Co1–S31	112.22(4)	113.07(3)	0.85	106.71(6)
S11–Co1–S41	108.21(4)	112.27(3)	2.71	114.46(5)
S21–Co1–S31	114.98(4)	108.23(3)	2.02	109.79(5)
S21–Co1–S41	102.32(4)	103.10(3)	0.78	110.04(5)
S31–Co1–S41	114.03(4)	114.33(3)	0.3	106.36(5)

^a Δ represents the deviation observed in the bond lengths and bond angles between **2** and **3**. The close structural resemblance of **2** (red trace) and **3** (green trace) can be visualized in the figure (see above).

structural isomorphs are expected to possess similar SH parameters (Table 3 vide infra).

Apart from the structural deviation/resemblance observed in all of the complexes, we analyzed their packing diagram to better understand the supramolecular interactions. In all of the complexes (**1–4**), both inter- and intramolecular hydrogen-bonding networks are spread across all directions. The closest $\text{Co}^{\text{II}}\cdots\text{Co}^{\text{II}}$ distances were found to be equal to 7.215, 6.803, 6.980, and 6.145 Å in complexes **1–4**, respectively (Figures 2, 3, and S5 and S6). As pointed out earlier, there are two crystallographically independent molecules in the unit cell of **1**; the closest $\text{Co}^{\text{II}}\cdots\text{Co}^{\text{II}}$ distance in **1a** \cdots **1a** is 7.215(5) Å, and that in **1b** \cdots **1b** is 7.561(2) Å.

There are two separate intermolecular distances [**1a** \cdots **1b** equal to 8.754(4) and 9.794(6) Å] for the two molecules in the asymmetric unit. The nitrate anions and solvate molecules reside between **1a** and **1b**. Because complexes **2** and **3** possess similar unit cell parameters, a representative packing diagram of **2** is shown in Figure 2. Although complexes **1–3** crystallize in a monoclinic crystal system, the space group for **1** (Pc) is different from that of **2** or **3** ($P2_1/c$). This results in a significant difference in the packing diagrams of the molecules, particularly the anion orientation. As observed in **1**, **2**, or **3**, arrays of cobalt(II) molecules are organized parallel to the c axis. The next set of arrays is generated by a 2_1 screw axis and a c glide, which are again parallel to the c axis.

The bromide (iodide in the case of **3**) ions are located between the two arrays (green dots in Figures 2 and S5). The location of the anions in **2** or **3** clearly follows a zigzag fashion because of the presence of a glide plane perpendicular to the screw symmetry axis (see the packing diagram of **2** or **3** in Figure 2), which is not the case for **1** (Figure S6). The change in the packing diagram of **2** or **3** is due to the halide anions

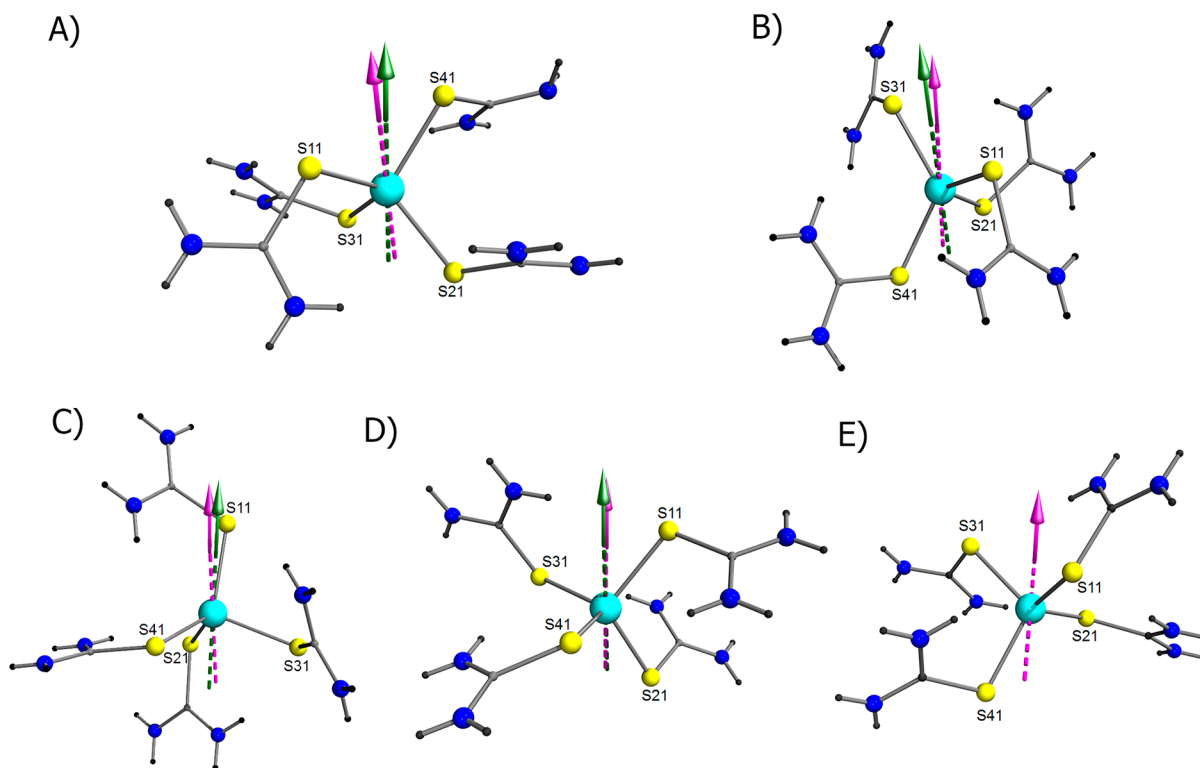


Figure 1. Ball-and-stick representation of the crystal structure of two crystallographically distinct molecules of **1** [**1a** (panel A) and **1b** (panel B)]. (C–E) Ball-and-stick representations of the crystal structures of complexes **2–4**,⁶¹ respectively. The magenta and green arrows on each of the complexes represent the computed D_{zz} orientation obtained from the calculations performed without and with anions along with the $[\text{Co}(\text{L}_1)]^{2+}$ core, respectively. Color code: sky blue, Co^{II} ; yellow, S; blue, N; gray, C; black, H.

compared to **1**. Because of the change in the position of the anions in the crystal lattice of **2** or **3**, the orientations of the L_1 ligands in **2** or **3** differ significantly compared to **1**. Anion-induced structural changes have been noticed in the coinage metal containing thiourea ligands reported by Eldik and co-workers.⁶² The anion-induced change in the orientation of L_1 in these complexes reduce the overall symmetry of cobalt(II) complexes, which has nonzero influence on the ZFS parameters, which indeed affects the magnetization relaxation dynamics of these complexes (vide infra). In both **2** and **3** as in **1**, two types of hydrogen bonding are present between (i) the proton of the amine group and the halide [Br (**2**) and I (**3**)] and (ii) the proton of the amine group and the ligating sulfur atom of the same molecule or a different molecule.

Although the metal core $[\text{Co}(\text{L}_1)_4]^{2+}$ of **4** is structurally analogous to that of **2** or **3**, the unit cell of this complex is different (Table 1). Hence, it is not surprising to have a distinct packing diagram for this complex (Figure 3). A packing diagram view along the b axis of **4** clearly shows that an array of molecules is arranged parallel to the a axis (unlike the cases in **2** or **3**). Between the two layers, SiF_6 anions reside in the lattice along the a axis. The closest $\text{Co}^{\text{II}}\cdots\text{Co}^{\text{II}}$ distance was found to be 6.2 Å. The fluorine atoms of the SiF_6 ion are involved in hydrogen bonding with the amine proton of L_1 . In addition to the anion-mediated hydrogen bonding between the molecules, inter- and/or intramolecular hydrogen bonding was observed between the sulfur atoms and amine protons of the molecules. The strength of hydrogen bonding varies (donor \cdots acceptor distance range of 2.8–3.358 Å) among all of the complexes (**1–4**), and the atoms involved in both inter- and

intramolecular hydrogen bonding for **2–4** are listed in Tables S2–S4.

EPR STUDIES

We and others have established already that an easy axis of magnetic anisotropy will be stabilized when a tetrahedral cobalt(II) ion is surrounded by soft donor atoms such as sulfur,^{36–38,40,41,45,63} an important factor that determines slow relaxation of magnetization. We have performed X-band EPR measurement on both pure and magnetically diluted samples of **1**, **2**, and **4** at 5.0 K, in order to determine the sign of D , if not its quantitative magnitude, because for the mononuclear cobalt(II) system the single-ion anisotropy tends to be greater than $h\nu$ in X-band EPR ($\sim 0.3 \text{ cm}^{-1}$) compared to the oligomeric paramagnetic complexes.^{64–66} As stated earlier in the previous section, complexes **2** and **3** are structural isomorphs of each other. This is also qualitatively reflected in the X-band EPR spectrum of pure polycrystalline samples of **2** and **3**; i.e., the EPR spectra recorded at 5.0 K (for both **2** and **3**) are similar to each other (Figure S7). On the other hand, pure samples of complexes **1** and **4** show a very broad signal between 1000 and 4000 Oe (data not shown). This is due to dipolar interactions, which are usually observed. To circumvent this effect, we studied the magnetically diluted solid solutions (10%) of **1**, **2**, and **4** (Figure 4).

The EPR spectrum of the 10% diluted sample of **1** shows a well-resolved EPR signal only in the g_{\parallel} region along with the nuclear hyperfine interaction ($I_{\text{Co}^{\text{II}}} = 7/2$), while the signal that corresponds to g_{\perp} was absent (Figure 4A).^{36,37,39,63,67,68} This is consistent with a negative D value for **1**. Similar to **1**, complex **4** also shows an EPR signal only in the g_{\parallel} region, but the

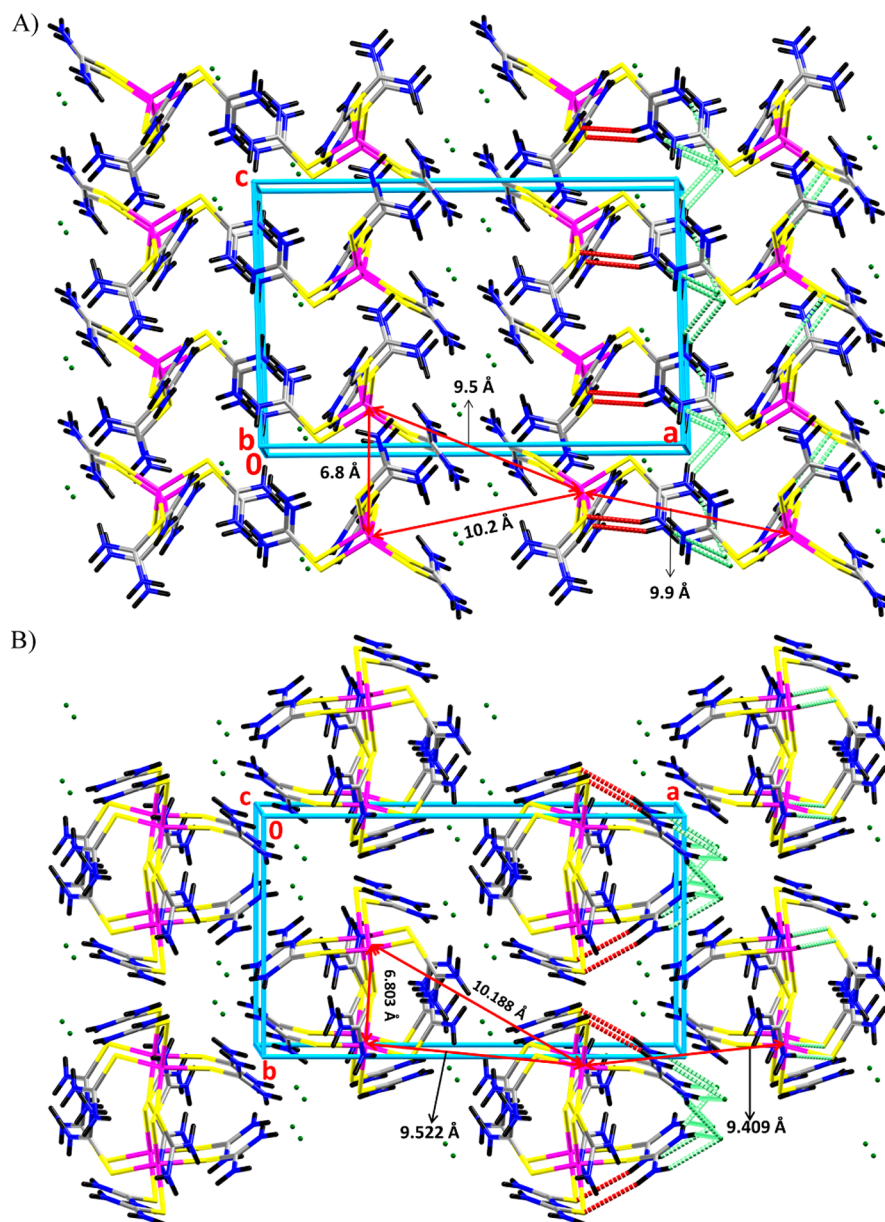


Figure 2. Packing diagrams of complex 2: (A) along *b* axis; (B) along the *c* axis. Dotted maroon lines represent intramolecular hydrogen bonding, whereas green dotted lines represent intermolecular hydrogen bonding. Color scheme: pink, Co^{II}; yellow, S; gray, C; blue, N; dark green, Br; black, H.

hyperfine interaction is not resolved (Figure 4C). This is, also, consistent with a negative *D* value for 4 like that for 1.^{36,37,39,67,68} A 10% magnetically diluted sample of 2 shows three well-resolved EPR signals (Figure 4B); however, the hyperfine interaction is not well-resolved in the low-field regime. Considering an effective spin value of $S = 1/2$, the EPR spectrum was simulated using the *EasySpin* software (version 5.2.16).⁶⁹

The experimental data are well reproduced by considering $g_x = 1.25$, $g_y = 1.62$, and $g_z = 5.8$ and the hyperfine coupling constant values of $A_x = 5$ MHz, $A_y = 10$ MHz, and $A_z = 700$ MHz with Gaussian and Lorentzian linewidths of 9 and 6 mT, respectively. The observation of $g_z \gg g_x$ and g_y is consistent with a negative *D* value for 2, as observed for the other complexes.^{70–72} Despite several attempts, the preparation of a magnetically diluted solid solution of 3 failed. Therefore, high-field HF-EPR measurements were carried out on a

representative complex 3 because complex 2 structurally resembles 3, and they are presumably expected to have similar SH parameters, which is well documented in the [Theoretical Studies on 1–4](#) section (*vide infra*).

HF-EPR STUDIES

HF-EPR measurements were carried out on a pure polycrystalline (100%) sample powder of 3 aligned with the applied magnetic field (see the [Experimental Section](#)). Depending on the frequency, four different resonance features are observed at $T = 2$ K (see [Figure S8](#) for details). The spectra exhibit strong field-dependent mixing of the phase and amplitude signal, which prevents the appropriate phase correction of the spectra. However, because the experimental setup enables detection of both the phase and amplitude of the signals, the actual resonance fields can be well read-off, thereby enabling precise

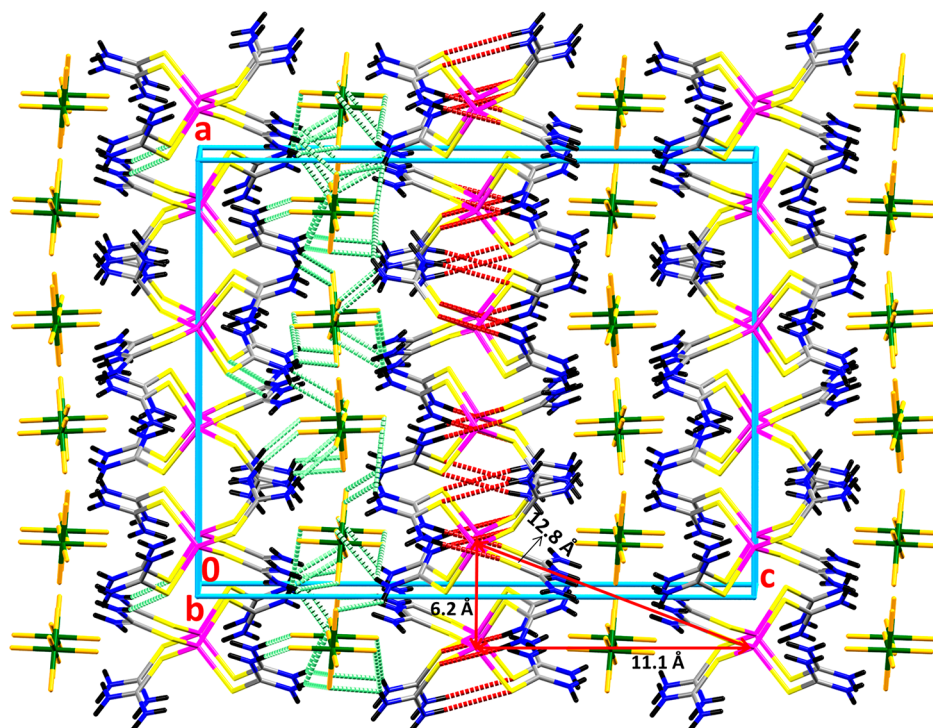


Figure 3. Packing diagram of complex 4. Dotted maroon lines represent intramolecular hydrogen bonding, whereas green dotted lines represent intermolecular hydrogen bonding. Color scheme: pink, Co^{II}; yellow, S; gray, C; blue, N; dark green, Si; orange, F; black, H.

determination of the resonance frequency-field diagram (Figure 5).

Figure 5 displays the temperature evolution of the HF-EPR spectra measured at 278.6 and 396.6 GHz, respectively. As will be shown below, the chosen frequencies surround the value of the EPR gap at zero field; i.e., $\Delta = 306$ GHz. The gap at zero field, denoted Δ , is the signature of an energy difference between the m_S sublevels and corresponds to $2D$ for an $S = 3/2$ spin state. At 396.6 GHz, three resonance features are present. Resonance features R1 and R3 are most pronounced at 2 K but significantly decrease in intensity upon heating and vanish at 30 and 50 K, respectively. The much weaker resonance R2 observed at the shoulder of R1 becomes invisible at 8 K. Meanwhile, below Δ , at 278.6 GHz, the resonances R1, R3, and R4 are clearly visible in the spectra (Figure 5a). As the temperature increases, resonance R3 gradually vanishes and completely disappears at 10 K, while the intensity of resonance R4 slightly increases between 2 and 6 K and remains up to 15 K.

A summary of all resonance features observed at different frequencies in the field range $1 \text{ T} \leq B \leq 16 \text{ T}$ shown in Figure 6 clearly confirms the presence of four distinct resonance branches R1–R4. In particular, for branches R2–R4, a linear behavior is clearly visible. While R1 and R2 exhibit gaps at zero field (Δ) of more than 300 GHz, R3 and R4 show $\Delta \approx 0$, implying that they are associated with transitions within a Kramers' doublet. In addition, the slopes of the branches allow one to attribute R2 and R4 to allowed transitions. Specifically, the slopes imply a g value of $g_{\text{eff}} = 2.00(5)$, suggesting that $\Delta m_S = \pm 1$. In contrast, branches R1 and R3 show much steeper slopes with $g_{\text{eff}} \neq 2$, indicating that they are forbidden resonances. To be specific, $g_{\text{eff}} = 4$ of resonance R1 may be associated with $\Delta m_S = \pm 2$ and $g_{\text{eff}} = 6$ of resonance R3 with $\Delta m_S = \pm 3$.

A quantitative analysis of the frequency-field diagram can be done by simulating the resonance branches by means of the Hamiltonian shown in eq 1.

$$H = g_B \vec{H} \cdot \vec{S} + D \left[S_z^2 - \frac{S(S+1)}{3} \right] + E(S_x^2 - S_y^2) \quad (1)$$

Simulation with the parameters $g = 2.00(5)$ and $|D| = 5.107 \text{ cm}^{-1}$ (and $E = 0$) yields the four branches shown in Figure 6 (see Figure S9 for more details). The simulated branches are in good agreement with the experimental data. The observed gap at zero field of the transitions between the different doublet states, i.e., between $m_S = \pm 3/2$ and $\pm 1/2$, amounts to $\Delta = 306(4)$ GHz [$10.20(14) \text{ cm}^{-1}$]. The fact that R3 is more pronounced than R4 indicates the negative sign of the single-ion anisotropy parameter D . The negative sign is further corroborated by the observed temperature dependence of the resonance intensities. Specifically, the spin-state transitions associated with resonances R1–R4 are $| -3/2 \rangle \rightarrow | +1/2 \rangle$ ($| +3/2 \rangle \rightarrow | -1/2 \rangle$) for R1, $| -3/2 \rangle \rightarrow | -1/2 \rangle$ ($| +3/2 \rangle \rightarrow | +1/2 \rangle$) for R2, $| -3/2 \rangle \rightarrow | +3/2 \rangle$ for R3, and $| -1/2 \rangle \rightarrow | +1/2 \rangle$ for R4. Transitions in the parentheses are associated with a measurement frequency below the gap at zero field. For microwave frequencies smaller than Δ , our model hence suggests that R3 is associated with a ground-state transition, while R1 and R4 arise from excited states, as indeed is suggested by the experimental data in Figure 5a. In contrast, for frequencies exceeding Δ , R1 and R2 become visible ground-state transitions, which are confirmed by the fact that maximum intensities are observed at the lowest temperature (Figure 5b). This assignment agrees with the observed temperature dependence, which tentatively suggests that R1 and R3 are ground-state transitions.

The HF-EPR data do not enable one to precisely quantify the transverse anisotropy parameter E of complex 3. However,

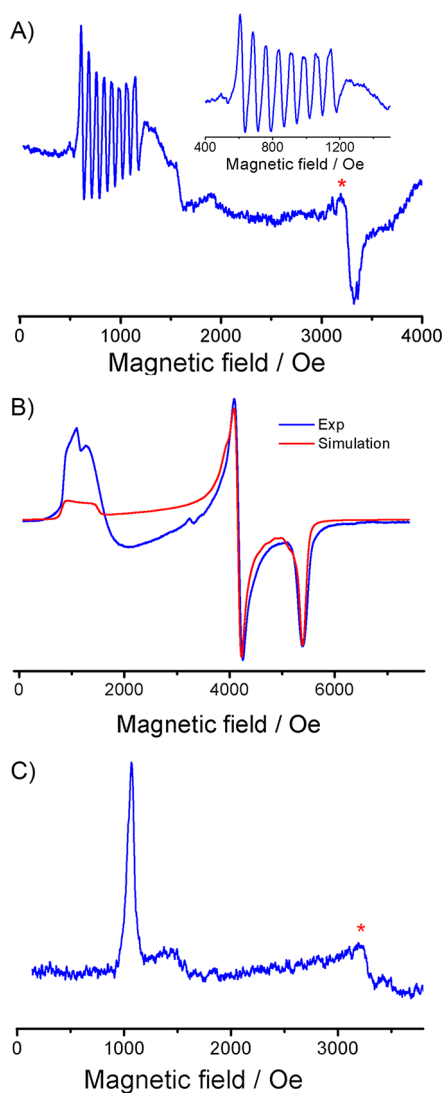


Figure 4. X-band EPR spectra of magnetically diluted solutions (10%) of complexes **1** (A), **2** (B), and **4** (C) performed at 5 K. The blue traces in all of the parts represent the experimental EPR spectra. Inset in part A: zoomed-in $g_{||}$ region showing the nuclear hyperfine coupling of cobalt(II). Experimental conditions: for **1**, frequency = 9.3834 GHz, microwave power = 13 dB, and modulation amplitude = 0.1 mT; for **2**, frequency = 9.3744 GHz, microwave power = 16 dB, and modulation amplitude = 0.1 mT; for **4**, frequency = 9.3681 GHz, microwave power = 18 dB, and modulation amplitude = 0.1 mT. The red trace in part B is the simulation of the experimental spectrum using the parameters described in the main text. Linewidth used [9, 6] for simulation. The asterisks in parts A and C denote the EPR signals that arise from the resonator cavity.

the presence of pronounced forbidden resonances implies vigorous spin-state mixing due to finite transverse anisotropy in the complex.⁷³ The effect of finite $E = 10$ GHz (0.33 cm^{-1}) on the simulated resonance branches is shown by dashed lines in Figure 6. The incorporation of the rhombic term $E(S_x^2 - S_y^2)$ (eq 1) yields nonlinear behavior of branch R1 at low energies as well as anticrossing effects of branches R2/R3 and R2/R4. Larger values of E are not compatible with the experimental data, so that $E = 10$ GHz sets an upper limit of transverse anisotropy. Finite E , however, does not cover a small but finite negative offset Δ of resonance branch R3, which might be associated with finite intermolecular magnetic interaction.

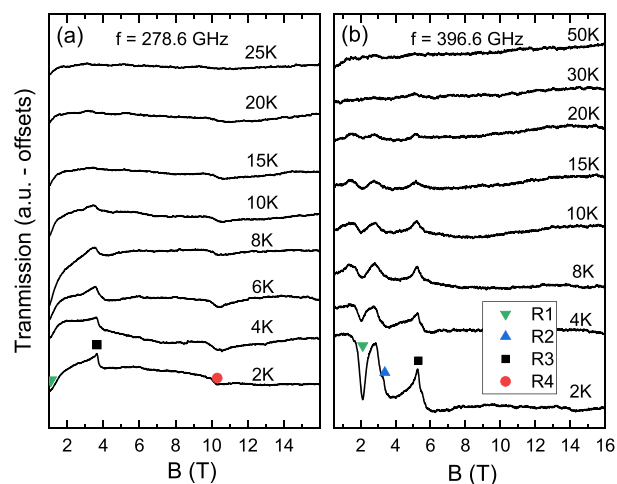


Figure 5. HF-EPR spectra of **3** (100% polycrystalline sample) measured at (a) $f = 278.6$ GHz and (b) $f = 396.6$ GHz at various temperatures. Symbols denote the corresponding resonance branches R1 to R4 (cf. Figure 6).

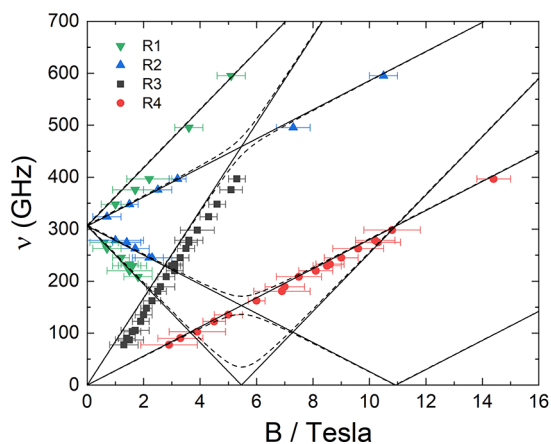


Figure 6. HF-EPR absorption frequencies versus magnetic field at $T = 2$ K. Solid lines show simulation results obtained by solving eq 1 with the *EasySpin*⁶⁹ software package using the parameters $S = 3/2$, $g = 2.00$, $D = 153$ GHz (5.1 cm^{-1}), and $E = 0$. Dashed lines indicate the effect of finite transverse anisotropy $E = 10$ GHz (0.33 cm^{-1}).

Overall, the HF-EPR experiments performed on **3** clearly reveal the negative anisotropy associated with the ground state and also enable quantitative determination of the zero-field energy gap [$2D = -10.20(14)\text{ cm}^{-1}$].

Direct-Current (dc) Magnetic Susceptibility Data of Complexes 2–4. dc magnetic susceptibility data were collected on the polycrystalline powders of **2–4** in the temperature range of 2–300 K in the presence of an external magnetic field of 10 kOe. The room temperature $\chi_M T(T)$ values of 2.26, 2.34, and $2.22\text{ cm}^3\text{ K mol}^{-1}$ were observed for complexes **2–4**, respectively (Figure 7); they correspond to those expected for high-spin cobalt(II) complexes, where the g value is larger than 2. $\chi_M T(T)$ tends to decrease slightly upon lowering of the temperature to 50 K, below which it suddenly drops and reaches values that remain larger than $1\text{ cm}^3\text{ K mol}^{-1}$ at $T = 2$ K. This sudden drop can be assigned to ZFS and/or intermolecular antiferromagnetic coupling. Field-dependent magnetization data were collected in the temperature range of 2–8 K for complexes **2–4** by sweeping the external magnetic field up to 70 kOe. There is no clear

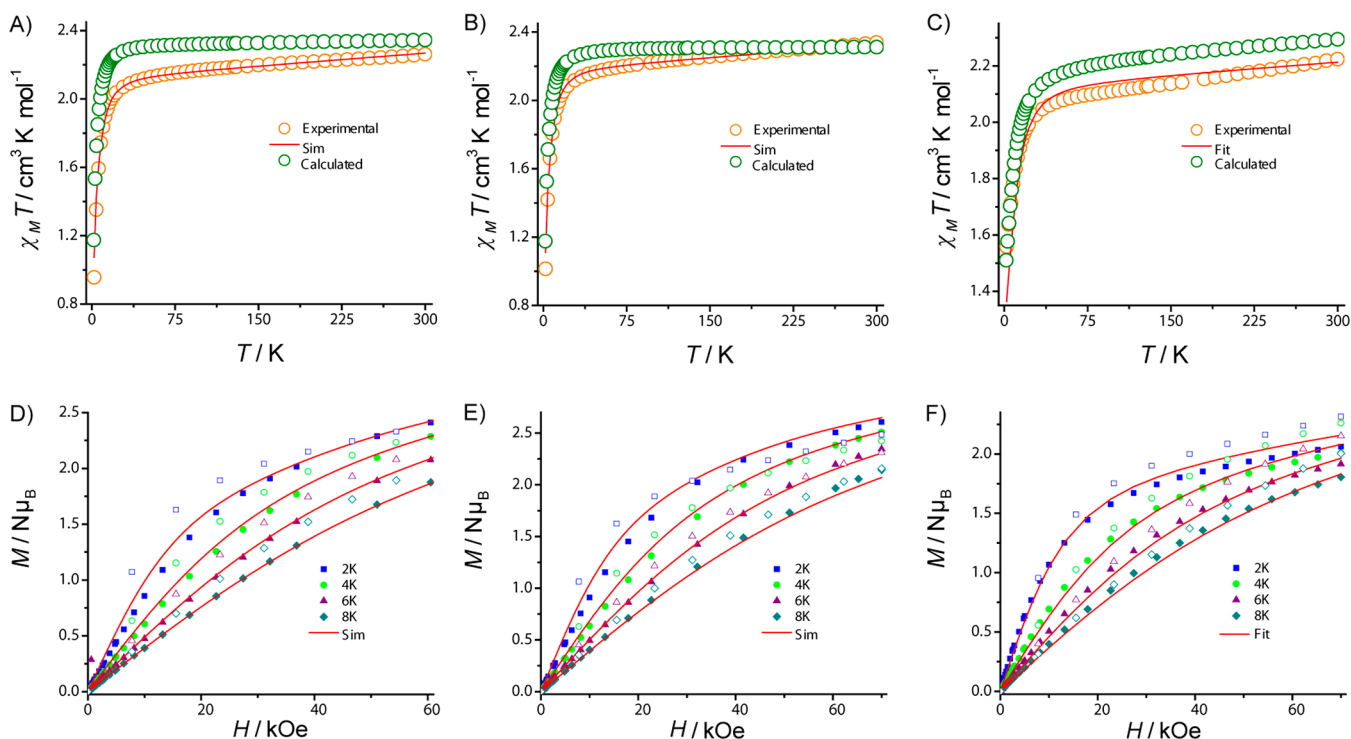


Figure 7. (A–C) dc magnetic susceptibility measurement performed on the polycrystalline sample of complexes 2–4, respectively, in the presence of an external magnetic field of 10 kOe. (D–F) Field-dependent magnetization measurements of complexes 2–4, respectively, performed at the indicated temperatures. Solid red traces represent the simulations of $\chi_M T(T)$ and $M(H)$ using the parameters extracted from HF-EPR for 2 and 3. For 4, the solid line denotes the simultaneous fit of $\chi_M T(T)$ and $M(H)$ (PHI software²⁵) using the parameters described in the main text. The open symbols in both the top (green) and bottom panels denote simulations of the magnetic data [$\chi_M T(T)$ and $M(H)$] using the SH parameters extracted from ab initio calculations using the parameters described in the main text.

Table 3. SH Parameters Extracted from CASSCF(NEVPT2)^a and PHI Fitting^b Results of the Experimental Data along with the Structural Factors That Influence The D Values

complex	D_{cal}^a (cm ⁻¹)	$ E/D ^a$	g_x, g_y, g_z^a	D^b (cm ⁻¹)	$ E/D ^b$	g_x, g_y, g_z^b	TIP (cm ³ mol ⁻¹)	2θ (deg) ^c	ω (deg) ^c
1a	-55.1	0.04	2.09, 2.16, 2.78	-61.7				93.3	10.7
1b	-43.4	0.03	2.12, 2.16, 2.66					93.2	17.9
2	-6.7	0.09	2.23, 2.22, 2.27	-5.9	0.06	2.15, 2.2, 2.0	5.8×10^{-4}	111.6	26.9
3	-5.0	0.19	2.24, 2.23, 2.27	-5.1 ^d	0.06 ^d	2.19, 2.2, 2.0 ^d	7.1×10^{-4}	110.3	27.5
4	-7.2	0.19	2.14, 2.19, 2.28	-12.2	0.16	2.13 (g_{iso})	3.0×10^{-4}	111.5	39.0

^aParameters computed from NEVPT2 calculations. ^bParameters extracted from PHI simulation/fitting. ^cThe 2θ and ω parameters observed in complexes 1–4 are also listed. They are defined in Figure 11A, which can provide details. ^dParameters extracted from HF-EPR.

indication for saturation of the magnetic moment even at 70 kOe at 2 K for the three complexes. The magnetic moments reaches final values of 2.45, 2.6, and 2.05 $N\mu_B$ at 2 K for complexes 2–4, respectively (Figure 7). A magnetic moment value well below 3 $N\mu_B$ at high field implies the presence of significant ZFS of the $S = 3/2$ state associated for these complexes. This is further strongly corroborated by the nonoverlapping signature of the reduced magnetization curves (Figure S10) of all complexes 2–4.

The magnetization and susceptibility data of 3 were simulated by fixing the SH parameters obtained from a HF-EPR study ($D = -5.1$ cm⁻¹, $E = 0.33$ cm⁻¹, and $g_z = 2.0$). A fairly good fit is obtained with $g_x = 2.19$, $g_y = 2.2$, and $\text{TIP} = 7.1 \times 10^{-4}$ cm³ mol⁻¹ (Figure 7 and Table 3). It is worth noting that a range set of parameters may lead to a fair fit of the data, as shown in Figure S11; the HF-EPR parameters are within this range.

Simulating the magnetic data of compound 2 with similar sets of the SH parameters (Figure S11; as in 3) leads to the

conclusion that its D value is in the same range for 3 (Table 3), which is consistent with the observation that similar X-band EPR spectra are observed for pure polycrystalline samples of 2 and 3. As anticipated, the SH parameters extracted from simulation of the magnetic data of 2 and 3 marginally differ from each other because both complexes are structural isomorphs of each other, as pointed out in the crystallographic section (Figure 7 and Table 3). The observed minor differences (in the extracted SH parameters) are attributed to the slight variation in the bond angles and bond lengths observed in these two complexes (refer to Table 2 for details). More importantly, the calculations performed on these molecules captured the observed scenario elegantly, and the computed SH parameters are in well agreement with the parameters extracted from magnetic data simulation and HF-EPR (vide infra).

Similarly, the magnetic data of $\chi_M T(T)$ and $M(B)$ of 4 were fitted simultaneously using isotropic g value (PHI software)²⁵ results in good agreement between the fit and experimental

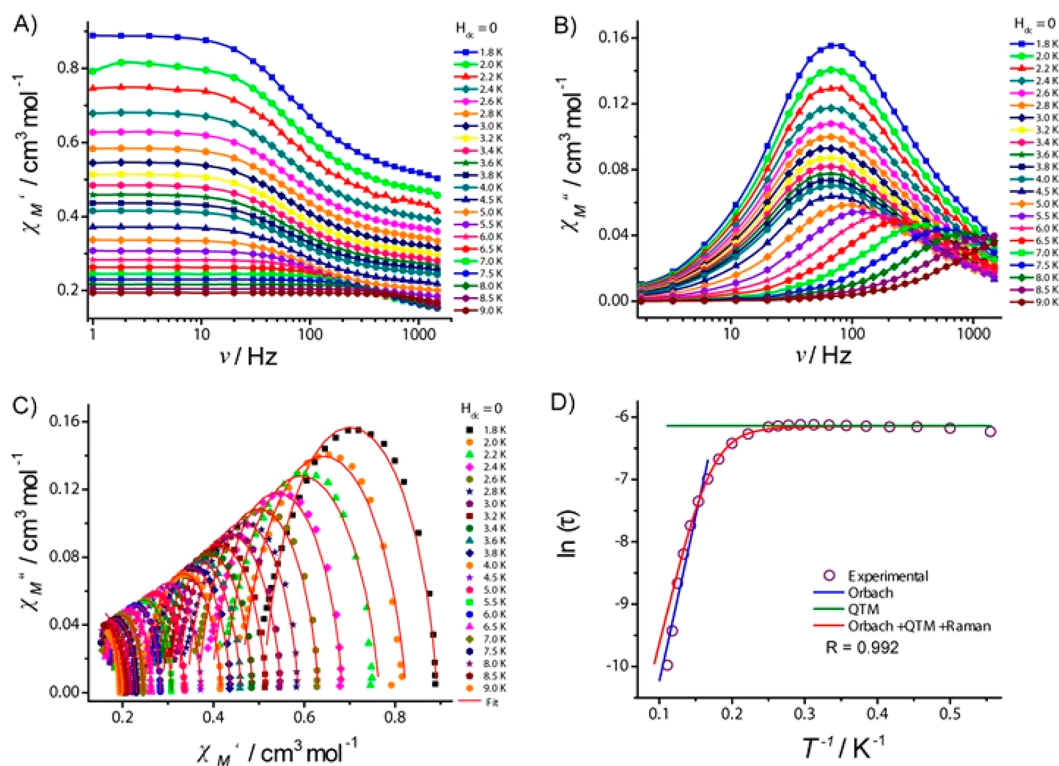


Figure 8. Frequency dependence of the (A) in-phase and (B) out-of-phase components of the ac susceptibility in the absence of an external magnetic field. (C) Cole–Cole plot of 3. (D) Arrhenius plot of complex 3.

magnetic data. The parameters obtained by the simulation/fit for all of the complexes are shown in Table 3.

The SH parameters reported for **1** are given in Table 3 for comparison purposes. The negative D value for **1** responsible for the easy axis of magnetization was confirmed earlier by the presence of a zero-field out-of-phase susceptibility signal and a magnetic hysteresis loop.³⁷ The negative D values for complexes **2–4** (Table 3) are also consistent with the presence of an easy axis of magnetization,^{42,43} although less robust than that for **1**. The sign of D associated with complexes **1**, **2**, and **4** was confirmed by X-band EPR spectroscopy, while for **3** frequency-dependent out-of-phase susceptibility signals ($H_{dc} = 0$) and high-field EPR unambiguously validate the negative sign for D and, consequently, the easy axis of magnetization associated with it (vide infra).

Among all four complexes, complex **1** is found to have the largest negative D value, while for the structurally analogous complexes **2–4**, D is less negative. This is due to a structural change of the coordination sphere of the cobalt(II) ions induced by the anion present in the crystal lattice (vide infra), which has been rationalized with the aid of theoretical calculations (vide infra).

Alternating-Current (ac) Susceptibility Measurements. Ac susceptibility measurements were carried out for complexes **2–4** (the ac susceptibility measurements for complex **1** have been reported elsewhere³⁷) in the absence and presence of an external optimum dc field with a 3 Oe ac oscillating field in the frequency range of 1–1500 Hz and in the temperature range of 1.8–10 K. In contrast to **1**, only a tiny out-of-phase susceptibility (χ_M'') signal is observed for both **2** and **4** even in the presence of an external dc magnetic field (Figure S12). A significant change in the relaxation phenomenon of **2** and **4** is attributed to the weaker $|D|$ value in

these complexes compared to **1**, which reduces the contribution of the Orbach process in comparison to other processes such as quantum tunneling of magnetization (QTM; due to possible dipolar/hyperfine interactions) and/or Raman that may operate. The application of an external magnetic field does not improve the situation (Figure S12), in line with the presence of a significant Raman process that speeds up the relaxation of magnetization.

In contrast to the relaxation dynamics phenomenon observed in **2** or **4**, complex **3** shows frequency-dependent out-of-phase susceptibility signals in the absence of an external magnetic field, suggesting magnetization blockade. The data in Figure 8 are consistent with a single relaxation process. At low temperature (<3 K), $\chi_M'' = f(\nu)$ curves are temperature-independent, in line with the presence of QTM/intermolecular interactions, while above 3 K, frequency- and temperature-dependent χ_M'' signals are observed in the temperature range measured. The Cole–Cole data were fitted considering a single relaxation using the generalized Debye model (eq 2)

$$\chi_{ac}(\omega) = \chi_S + \frac{\chi_T - \chi_S}{1 + (i\omega\tau)^{1-\alpha}} \quad (2)$$

where χ_S = adiabatic susceptibility, χ_T = isothermal susceptibility, ω = angular frequency, τ = relaxation time, and α reflects the extent of distribution of the relaxation times.

The α values range from 0.12 (1.8 K) to 0.08 (9.0 K). The τ values obtained through the fitting of Cole–Cole plots were employed to construct the Arrhenius plot. The entire temperature range of the $\ln(\tau) = f(1/T)$ plot was fitted by considering various relaxation processes (eq 3).

$$\frac{1}{\tau} = \frac{B_1}{1 + B_2 H^2} + A H^2 T + C T^n + \frac{1}{\tau_0} \exp\left(\frac{-U_{\text{eff}}}{k_B T}\right) \quad (3)$$

Table 4. NEVPT2-Computed SH Parameters (g , D , and $|E/D|$) along with Listed State-by-State Contributions to the D and E Values^a

state	1a			1b		
	energy (cm ⁻¹)	contribution to D (cm ⁻¹)	contribution to E (cm ⁻¹)	energy (cm ⁻¹)	contribution to D (cm ⁻¹)	contribution to E (cm ⁻¹)
⁴ T ₂ (F)	1323.5 (1284.8)	-75.41 (-77.50)	-0.01 (-0.05)	1655.5 (1695.1)	-63.04 (-61.73)	-0.019 (-0.003)
	5552.0 (5773.4)	9.56 (8.80)	-9.69 (-9.31)	6078.1 (6066.7)	8.33 (6.61)	-8.42 (-6.64)
	7179.8 (7410.4)	1.36 (0.81)	1.08 (0.82)	7203.2 (7239.7)	4.48 (4.92)	4.22 (3.85)
state	2			3		
	energy (cm ⁻¹)	contribution to D (cm ⁻¹)	contribution to E (cm ⁻¹)	energy (cm ⁻¹)	contribution to D (cm ⁻¹)	contribution to E (cm ⁻¹)
⁴ A ₁ (F)	4313.0 (4535.6)	-25.42 (-18.71)	0.36 (-2.31)	4364.7 (4541.1)	-21.82 (-20.76)	0.07 (1.40)
⁴ E(F)	5114.4 (5137.4)	8.53 (6.62)	9.67 (5.19)	4919.6 (5003.9)	11.04 (9.29)	-4.77 (-6.79)
		10.47 (4.94)	-10.67 (-4.10)	5095.2 (5248.5)	5.96 (7.30)	3.70 (4.59)
state	4					
	energy (cm ⁻¹)	contribution to D (cm ⁻¹)	contribution to E (cm ⁻¹)			
⁴ A ₁ (F)	4306.7 (4466.6)	-19.24 (10.76)	-0.67 (11.83)			
⁴ B ₁ (F)	4918.3 (5042.8)	3.95 (7.41)	-8.61 (-9.61)			
⁴ B ₂ (F)	6092.6 (6247.5)	7.80 (-10.92)	7.33 (0.02)			
	1a	1b	2	3	4	
D_{tot}	-55.14 (-58.89)	-43.40 (-43.25)	-6.77 (-7.19)	-5.00 (-4.48)	-7.23 (\pm 7.27)	
$ E/D $	0.04 (0.03)	0.03 (0.03)	0.09 (0.18)	0.19 (0.17)	0.22 (0.32)	
g_x	2.09 (2.08)	2.12 (2.11)	2.23 (2.19)	2.24 (2.21)	2.24 (2.17)	
g_y	2.16 (2.15)	2.16 (2.15)	2.22 (2.22)	2.23 (2.23)	2.19 (2.23)	
g_z	2.78 (2.79)	2.66 (2.64)	2.27 (2.29)	2.27 (2.74)	2.28 (2.27)	

^aThe SH parameters extracted from the calculations in the presence of anions are given in parentheses.

The first term on the right-hand side of the equation represents the QTM process, the second is the direct process, the third is the Raman process, and the last term denotes the Orbach process. Because the measurement is carried out in the absence of any external magnetic field, the entire temperature range can be fitted by employing Orbach, Raman, and QTM only using the parameters $U_{\text{eff}} = 34.8 \text{ cm}^{-1}$, $\tau_0 = 5 \times 10^{-7} \text{ s}$, $C = 0.01634 \text{ s}^{-1} \text{ K}^{-5}$, $n = 5$, and $B_1 = 0.00215 \text{ s}^{-1}$.

Although both the 2 and 3 X-ray structures and SH parameters marginally differ from one another, the drastic change in the slow relaxation of magnetization phenomenon observed in 3 compared to 2 is quite surprising. Hence, we carefully looked up the parameters extracted for 3, the effective energy barrier extracted for 3 (34.8 cm^{-1}) is significantly higher than the theoretically expected energy barrier [i.e., $|2D| = 10.2(14) \text{ cm}^{-1}$]. This suggests that the slow magnetization relaxation phenomenon observed for 3 is not of molecular origin but due to interactions involving several molecules (dipolar, for example). Strong intermolecular hydrogen bonding leading to long-range ordering has been observed in complex 1 studied earlier.³⁷ As mentioned in the EPR Studies section, our attempts to prepare magnetically diluted samples of complex 3, in order to investigate the effect of intermolecular interactions on the ac data, were not successful. For rationalization of the ZFS parameter, we will rely on the D value extracted from fitting of the magnetization data for 2 and 4 and from HF-EPR for 3.

Theoretical Studies on 1–4. In order to probe the origin of the weaker magnitude of D for complexes 2–4 compared to 1, we performed ab initio SA-CASSCF calculations using X-ray structures of the complexes. All of the molecules were oriented based on the approximate symmetry present in the first coordination sphere prior to calculations to obtain orbitals that are consistent with the ligand-field framework. Dynamic correlations were incorporated using the NEVPT2 method

available in ORCA 4.1. The obtained estimates of the SH parameters are very similar, and these are listed in Table 4. The obtained SH parameters obtained from CASSCF calculations are listed in Table S5. Because the experimental investigation mainly focuses on the influence of the anions on the SH parameters, calculations were performed with and without anions for all of the complexes (1–4), where the structures are reoriented in the canonical magnetic frame. However, we noticed that only a marginal difference is observed in the extracted SH parameters for 2 and 3 in comparison to 4. In the case of complex 4, the inclusion of anions in the calculations leads to $|E/D| = 0.33$ and therefore the sign of D cannot be unambiguously determined. However, the axial anisotropy nature of 4 is confirmed by X-band EPR measurements (vide supra). Therefore, further discussions will be based on the parameters extracted from the molecules where anions were not incorporated into the calculations. Computational studies of complex 1 were performed and reported by us earlier, and only for comparison purposes, the SH parameters and eigenvalue plots of 1 are recalled here.³⁷ The computed SH parameters are listed in Tables 3 and 4.

The computed magnetic data using the parameters extracted from NEVPT2 calculations are in good agreement with the experimental magnetic data [see Figure 7 for both $\chi_M T(T)$ and $M(H)$], offering confidence on the parameters extracted. In line with the experimental observation, the computed D values also follow a similar trend, i.e., $1 \gg 4 > 2 \sim 3$. Additionally, the CASSCF+RASSI-SO/SINGLE_ANISO procedure (Tables S5 and S6) also yields a similar set of D values.^{74–78}

Even though single-crystal XRD studies reveal that all three complexes possess distorted T_d geometry, in reality, complex 1 is close to D_{2d} (0.4), 2 (0.85) and 3 (0.82) possess C_{3v} , and 4 is close to C_{2v} (0.73) symmetry with respect to the second coordination sphere in all of the complexes. The numbers shown next to each symmetry is the deviation calculated from

the ideal D_{2d} (for **1**), C_{3v} (for **2** and **3**), and C_{2v} (for **4**) symmetry using *Chemcraft* software.⁷⁹ However, we would like to point out that the overall symmetry of all of the complexes is C_1 . The drastic change in the geometry around the cobalt(II) center is due to the disposition of the different anions present in the crystal lattice of the respective complexes. Lowering the symmetry from T_d to pseudo- D_{2d} , $-C_{3v}$, and $-C_{2v}$ lifts the degeneracy of the T_d first excited state (4T_2), as depicted in **Figures 9** and **10**. The mixing between the ground and excited

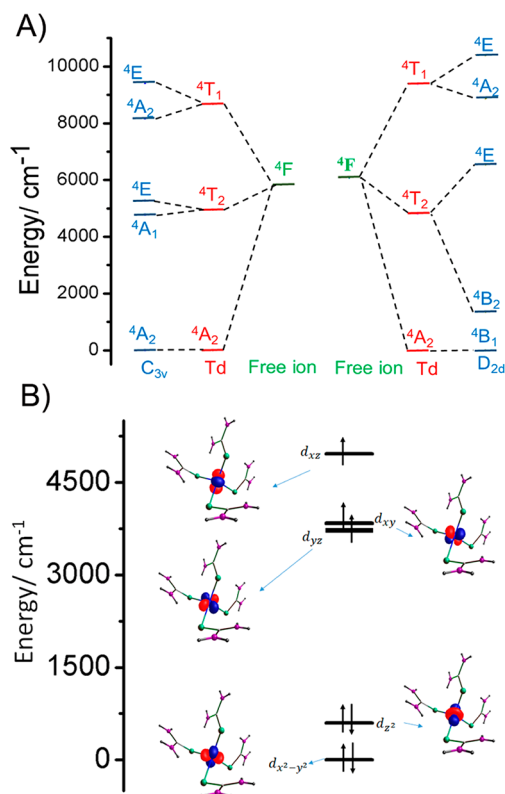


Figure 9. (A) CASSCF-computed energies of a low-lying quartet state for complex **2** (pseudo- C_{3v}), which consists of 25% contribution and **1** (D_{2d}) along with the ideal T_d complex. (B) CASSCF-computed eigenvalue plot for complex **2**.

states in these distorted geometries gives rise to a ZFS that is proportional to the degree of mixing. The contribution to D of each excited state is inversely proportional to its energy separation with the ground state. Thus, for **1**, the first excited state (D_{2d} symmetry) contributes negatively to D with ca. -100 cm^{-1} , while for the other complexes, this contribution is almost 3 times weaker (-30 cm^{-1} ; **Table 4**).^{37,38,42,43,80} The contribution of the other two excited states is positive (for the overall D value) and almost the same for the four complexes and much weaker than that of the first excited state. Thus, the origin of the larger overall $|D|$ value in **1** is attributed to the larger mixing between the ground and first excited states compared to **2–4**.

The sign of D can be understood by analyzing the wave function of each state. The ground state, as well as the first excited state, has multideterminantal characteristics for complexes **2–4**, and **Figures 9** and **10** show one of the major electronic configurations of the ground state for complexes **2** and **4**, respectively. For complex **2**, the first excited state has four dominant configurations with 27%, 25%,

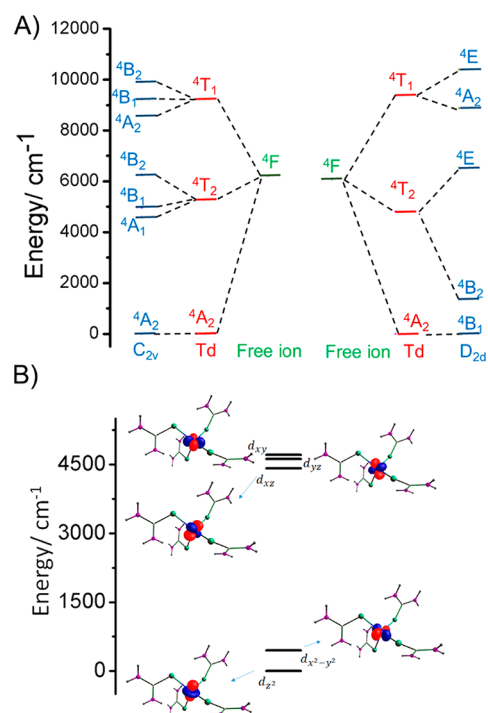


Figure 10. (A) CASSCF-computed energies of a low-lying quartet state for complex **4** (pseudo- C_{2v}), which consists of a 31% contribution and **1** (D_{2d}) along with the ideal T_d complex. (B) CASSCF-computed eigenvalue plot for complex **4**.

13%, and 15% contributions. Among these four configurations, the configurations with 25% and 13% weight contribute to a negative D , while the configuration with 15% weight contributes to a positive D . The most dominant configuration (27%) was found not to contribute to the net D value because of its $L_z = 0$. A similar analysis can be made for the other excited states and rationalizes well the sign of D .

In addition to the computed overall D , the computed $|E/D|$ values were found to increase in the order of $1 < 2 < 3 < 4$. A slight distortion from the D_{2d} symmetry can lift the degeneracy of the E states, which led to the increased rhombicity.⁴³ Complex **4** that has approximately C_{2v} possesses the largest E value (**Table 4**).³⁷

The lowest-energy transition in complexes **2–4** not only contributes to small negative D values but also to large E values compared to **1**. A similar trend is found in other spin-conserved transitions between orbitals with different $|m_l|$ values. The decreased D and increased $|E/D|$ values in complexes **2–4** trigger faster relaxation of magnetization. This is consistent with the experimental observation that complexes **2** and **4** do not show zero-field slow relaxation behavior.

Recently, we and others have pointed out that the structural parameters 2θ (first coordination sphere) and ω (second coordination sphere) play a major role in determining the sign and magnitude of magnetic ZFS in cobalt(II) tetrahedral complexes (**Figure 11A**). These studies show that symmetry lowering in T_d strongly splits the first excited state. A correlation was developed by varying the 2θ and ω parameters in the parent complex **1** reported elsewhere,³⁷ where a large negative D value is observed for small 2θ and ω parameters and an opposite trend is observed for the increased 2θ and ω values. For complexes **2–4**, the measured 2θ and ω parameters

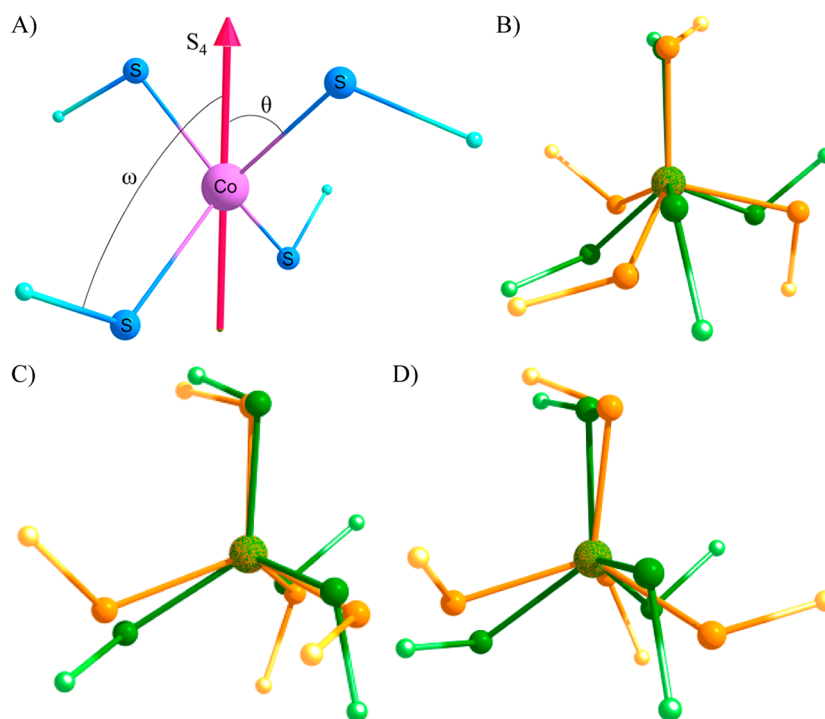


Figure 11. (A) Schematic representation of the first (2θ) and second (ω) coordination spheres of a cobalt(II) ion. Overlap of the crystal structures of (B) 2, (C) 3, and (D) 4 with 1 (green) showing the extent of distortion in complexes 2–4 (orange) with respect to complex 1.

are significantly higher than the value observed for 1 and, hence, a weak D value (Table 3). Earlier Neese et al. reported that, for π -anisotropic ligand systems such as sulfur, tetrahedral cobalt(II) complexes will lead to negative D values in the case of both elongated ($<109.47^\circ$) and compressed ($>109.47^\circ$, until 117°) tetrahedral distortions.^{37,43} Complex 1 is an example of a tetragonally elongated system ($\sim 2\theta = 93^\circ$), hence leading to large negative D value. On the other hand, the increased 2θ ($\sim 111^\circ$) and ω ($27\text{--}39^\circ$) values (compared to 1) for complexes 2–4 reduce the magnitude of the D value. A significant distortion in the metal coordination sphere of complexes 2–4 compared to 1 is due to the change of anions in the crystal lattice. The extent of distortion observed in the metal core of each complex (2–4) is compared with the parent complex 1 (Figure 11).

Overall, the present study reiterates the fact that not only the first coordination sphere but also the second coordination sphere possess a significant influence in determining both the sign and magnitude of D values in tetrahedral cobalt(II) complexes. Also, the study reveals that the anions in the crystal lattice indirectly modulate the D values by inducing distortion in the metal core through supramolecular interactions such as hydrogen bonding.

CONCLUSIONS

In conclusion, we have isolated a family of complexes with different counteranions with molecular formulas of $[\text{Co}(\text{L}_1)_4]\text{X}_2$ [$\text{X} = \text{NO}_3$ (1), Br (2), and I (3)] and $[\text{Co}(\text{L}_1)_4](\text{SiF}_6)$ (4), which are characterized by single-crystal XRD. The cobalt(II) ion in all of the complexes possess distorted tetrahedral geometry but the local geometry was found to be D_{2d} for 1 and C_{3v} and C_{2v} geometry (with respect to the second coordination sphere) for 2 (or 3) and 4, respectively. Experimental magnetic data reveal that all of the complexes possess negative ZFS parameters. Complex 1 possesses large D values with small $|E/D|$

$D|$ values compared to 2–4. Because of the preferable combination of large D and small $|E/D|$, 1 behaves as a zero-field SIM, while no χ_M'' signals were observed for both 2 and 4, even in the presence an external bias field. The drastic change observed in the SH parameters and relaxation dynamics of complex 1 compared to complexes 2–4 is correlated to the structural distortion, which is induced by different anions present in the crystal lattice of the respective complexes. The drastic reduction in ZFS in complexes 2–4 (compared to 1) is confirmed by HF-EPR data recorded on a representative complex 3. The SH parameters extracted for 3 through detailed HF-EPR analysis not only reveal the sign but also facilitate the determination of the magnitude of D quantitatively [$-5.1(7) \text{ cm}^{-1}$], which is consistent with the computed SH parameters. This reveals the reliability of the SH parameters computed for other complexes (1, 2, and 4). The trend observed experimentally for the D values ($1 \gg 4 > 2 \sim 3$) is rationalized using ab initio calculations considering the first coordination sphere (2θ) combined with the second coordination sphere (ω) effect, which is consistent with experimental observations. Overall, the study discloses that four-coordinate cobalt(II) with D_{2d} geometry tends to stabilize the large negative D value, while lowering the symmetry of the complex not only weakens the axiality but also increases the rhombicity.

ASSOCIATED CONTENT

Supporting Information

The Supporting Information is available free of charge on the ACS Publications website at DOI: 10.1021/acs.inorgchem.9b00632.

PXRD of all complexes, supporting magnetic data, field sweep ac data for 2–4, the basis set used for MOLCAS calculations, and the SH parameters extracted (PDF)

Accession Codes

CCDC 1878570–1878572 contain the supplementary crystallographic data for this paper. These data can be obtained free of charge via www.ccdc.cam.ac.uk/data_request/cif, or by emailing data_request@ccdc.cam.ac.uk, or by contacting The Cambridge Crystallographic Data Centre, 12 Union Road, Cambridge CB2 1EZ, UK; fax: +44 1223 336033.

AUTHOR INFORMATION

Corresponding Authors

*E-mail: talal.mallah@u-psud.fr (T.M.).

*E-mail: rajaraman@chem.iitb.ac.in (G.R.).

*E-mail: eswar@chem.iitb.ac.in (M.S.).

ORCID

Talal Mallah: 0000-0002-9311-3463

Gopalan Rajaraman: 0000-0001-6133-3026

Maheswaran Shanmugam: 0000-0002-9012-743X

Author Contributions

†These authors contributed equally.

Notes

The authors declare no competing financial interest.

ACKNOWLEDGMENTS

M.S. thanks the funding agencies SERB (Grant EMR/2015/000592), INSA (Grant SP/YSP/119/2015/1264), and CSIR [Grant 01(2933)/18/EMR-II] for financial assistance and the central facility IRCC, IIT Bombay, for access of the multifrequency EPR facility. M.S. also thanks Prof. Ashutosh Kumar, BSBE department, IIT Bombay, for his timely help with the solid-state NMR measurements. G.R. thanks SERB for funding (Grant CRG/2018/000430).

REFERENCES

- Gomez-Coca, S.; Cremades, E.; Aliaga-Alcalde, N.; Ruiz, E. Mononuclear Single-Molecule Magnets: Tailoring the Magnetic Anisotropy of First-Row Transition-Metal Complexes. *J. Am. Chem. Soc.* **2013**, *135* (18), 7010.
- Craig, G. A.; Murrie, M. 3d single-ion magnets. *Chem. Soc. Rev.* **2015**, *44* (8), 2135.
- Frost, J. M.; Harriman, K. L. M.; Murugesu, M. The rise of 3-d single-ion magnets in molecular magnetism: towards materials from molecules? *Chem. Sci.* **2016**, *7* (4), 2470.
- Sessoli, R.; Gatteschi, D.; Caneschi, A.; Novak, M. A. Magnetic bistability in a metal-ion cluster. *Nature (London, U. K.)* **1993**, *365* (6442), 141.
- Caneschi, A.; Gatteschi, D.; Sessoli, R.; Barra, A. L.; Brunel, L. C.; Guillot, M. Alternating current susceptibility, high field magnetization, and millimeter band EPR evidence for a ground $S = 10$ state in $[\text{Mn}_{12}\text{O}_{12}(\text{CH}_3\text{COO})_{16}(\text{H}_2\text{O})_4]\cdot 2\text{CH}_3\text{COOH}\cdot 4\text{H}_2\text{O}$. *J. Am. Chem. Soc.* **1991**, *113* (15), 5873.
- Bao, D.-X.; Xiang, S.; Wang, J.; Li, Y.-C.; Zhao, X.-Q. Review: Single-molecule magnets based on pyridine alcohol ligands. *J. Coord. Chem.* **2016**, *69* (21), 3131.
- Meng, Y.-S.; Jiang, S.-D.; Wang, B.-W.; Gao, S. Understanding the Magnetic Anisotropy toward Single-Ion Magnets. *Acc. Chem. Res.* **2016**, *49* (11), 2381.
- Murrie, M. Cobalt(ii) single-molecule magnets. *Chem. Soc. Rev.* **2010**, *39* (6), 1986.
- Mazarakioti, E. C.; Regier, J.; Cunha-Silva, L.; Wernsdorfer, W.; Pilkington, M.; Tang, J.; Stamatatos, T. C. Large Energy Barrier and Magnetization Hysteresis at 5 K for a Symmetric $\{\text{Dy}_2\}$ Complex with Spherical Tricapped Trigonal Prismatic Dy(III) Ions. *Inorg. Chem.* **2017**, *56* (6), 3568.
- Ding, Y.-S.; Chilton, N. F.; Winpenny, R. E. P.; Zheng, Y.-Z. On Approaching the Limit of Molecular Magnetic Anisotropy: A

Near-Perfect Pentagonal Bipyramidal Dysprosium(III) Single-Molecule Magnet. *Angew. Chem., Int. Ed.* **2016**, *55* (52), 16071.

(11) Langley, S. K.; Wielechowski, D. P.; Moubaraki, B.; Murray, K. S. Enhancing the magnetic blocking temperature and magnetic coercivity of $\{\text{CrIII}_2\text{LnIII}_2\}$ single-molecule magnets via bridging ligand modification. *Chem. Commun. (Cambridge, U. K.)* **2016**, *52* (73), 10976.

(12) Hernandez Sanchez, R.; Betley, T. A. Meta-Atom Behavior in Clusters Revealing Large Spin Ground States. *J. Am. Chem. Soc.* **2015**, *137* (43), 13949.

(13) Demir, S.; Zadrozny, J. M.; Nippe, M.; Long, J. R. Exchange coupling and magnetic blocking in bipyrimidyl radical-bridged dilanthanide complexes. *J. Am. Chem. Soc.* **2012**, *134* (45), 18546.

(14) Rinehart, J. D.; Fang, M.; Evans, W. J.; Long, J. R. A N23-Radical-Bridged Terbium Complex Exhibiting Magnetic Hysteresis at 14 K. *J. Am. Chem. Soc.* **2011**, *133* (36), 14236.

(15) Ruamps, R.; Batchelor, L. J.; Guillot, R.; Zakhia, G.; Barra, A.-L.; Wernsdorfer, W.; Guihery, N.; Mallah, T. Ising-type magnetic anisotropy and single molecule magnet behaviour in mononuclear trigonal bipyramidal Co(II) complexes. *Chem. Sci.* **2014**, *5* (9), 3418.

(16) Neese, F.; Pantazis, D. A. What is not required to make a single molecule magnet. *Faraday Discuss.* **2011**, *148*, 229.

(17) Frost, J. M.; Harriman, K. L. M.; Murugesu, M. The rise of 3-d single-ion magnets in molecular magnetism: towards materials from molecules? *Chem. Sci.* **2016**, *7* (4), 2470.

(18) Bar, A. K.; Pichon, C.; Sutter, J.-P. Magnetic anisotropy in two-to eight-coordinated transition-metal complexes: Recent developments in molecular magnetism. *Coord. Chem. Rev.* **2016**, *308*, 346.

(19) Gomez-Coca, S.; Aravena, D.; Morales, R.; Ruiz, E. Large magnetic anisotropy in mononuclear metal complexes. *Coord. Chem. Rev.* **2015**, *289–290*, 379.

(20) Craig, G. A.; Murrie, M. 3d single-ion magnets. *Chem. Soc. Rev.* **2015**, *44* (8), 2135.

(21) Tripathi, S.; Dey, A.; Shanmugam, M.; Narayanan, R. S.; Chandrasekhar, V. Cobalt(II) Complexes as Single-Ion Magnets. *Topics in Organometallic Chemistry*; Springer: Berlin, 2018;

(22) Poulten, R. C.; Page, M. J.; Algarra, A. G.; Le Roy, J. J.; Lopez, I.; Carter, E.; Llobet, A.; Macgregor, S. A.; Mahon, M. F.; Murphy, D. M.; et al. Synthesis, Electronic Structure, and Magnetism of $[\text{Ni}(\text{6-Mes})_2]^+$: A Two-Coordinate Nickel(I) Complex Stabilized by Bulky N-Heterocyclic Carbenes. *J. Am. Chem. Soc.* **2013**, *135* (37), 13640.

(23) Yao, X.-N.; Du, J.-Z.; Zhang, Y.-Q.; Leng, X.-B.; Yang, M.-W.; Jiang, S.-D.; Wang, Z.-X.; Ouyang, Z.-W.; Deng, L.; Wang, B.-W.; et al. Two-Coordinate Co(II) Imido Complexes as Outstanding Single-Molecule Magnets. *J. Am. Chem. Soc.* **2017**, *139* (1), 373.

(24) Zadrozny, J. M.; Xiao, D. J.; Atanasov, M.; Long, G. J.; Grandjean, F.; Neese, F.; Long, J. R. Magnetic blocking in a linear iron(I) complex. *Nat. Chem.* **2013**, *5* (7), 577.

(25) Chilton, N. F.; Anderson, R. P.; Turner, L. D.; Soncini, A.; Murray, K. S. PHI: A powerful new program for the analysis of anisotropic monomeric and exchange-coupled polynuclear d- and f-block complexes. *J. Comput. Chem.* **2013**, *34* (13), 1164.

(26) Eikeland, E.; Lock, N.; Filso, M.; Stingaciu, M.; Shen, Y.; Overgaard, J.; Iversen, B. B. Alkali Metal Ion Templated Transition Metal Formate Framework Materials: Synthesis, Crystal Structures, Ion Migration, and Magnetism. *Inorg. Chem.* **2014**, *53* (19), 10178.

(27) Karunadasa, H. I.; Arquero, K. D.; Berben, L. A.; Long, J. R. Enhancing the Magnetic Anisotropy of Cyano-Ligated Chromium(II) and Chromium(III) Complexes via Heavy Halide Ligand Effects. *Inorg. Chem.* **2010**, *49* (11), 4738.

(28) Smolko, L.; Černák, J.; Dušek, M.; Titiš, J.; Boča, R. Tetracoordinate Co(ii) complexes containing bathocuproine and single molecule magnetism. *New J. Chem.* **2016**, *40* (8), 6593.

(29) Smolko, L.; Černák, J.; Dušek, M.; Miklovič, J.; Titiš, J.; Boča, R. Three tetracoordinate Co(ii) complexes $[\text{Co}(\text{biq})\text{X}_2]$ (X = Cl, Br, I) with easy-plane magnetic anisotropy as field-induced single-molecule magnets. *Dalton Trans.* **2015**, *44* (40), 17565.

(30) Lin, P.-H.; Smythe, N. C.; Gorelsky, S. I.; Maguire, S.; Henson, N. J.; Korobkov, I.; Scott, B. L.; Gordon, J. C.; Baker, R. T.;

Murugesu, M. Importance of Out-of-State Spin–Orbit Coupling for Slow Magnetic Relaxation in Mononuclear FeII Complexes. *J. Am. Chem. Soc.* **2011**, *133* (40), 15806.

(31) Zhu, Y.-Y.; Zhang, Y.-Q.; Yin, T.-T.; Gao, C.; Wang, B.-W.; Gao, S. A Family of CoII/CoIII Single-Ion Magnets with Zero-Field Slow Magnetic Relaxation: Fine Tuning of Energy Barrier by Remote Substituent and Counter Cation. *Inorg. Chem.* **2015**, *54* (11), 5475.

(32) Ziegenbalg, S.; Hornig, D.; Goerls, H.; Plass, W. Cobalt(II)-Based Single-Ion Magnets with Distorted Pseudotetrahedral [N2O2] Coordination: Experimental and Theoretical Investigations. *Inorg. Chem.* **2016**, *55* (8), 4047.

(33) Schweinfurth, D.; Sommer, M. G.; Atanasov, M.; Demeshko, S.; Hohloch, S.; Meyer, F.; Neese, F.; Sarkar, B. The Ligand Field of the Azido Ligand: Insights into Bonding Parameters and Magnetic Anisotropy in a Co(II)-Azido Complex. *J. Am. Chem. Soc.* **2015**, *137* (5), 1993.

(34) Shao, F.; Cahier, B.; Rivière, E.; Guillot, R.; Guihéry, N.; Campbell, V. E.; Mallah, T. Structural Dependence of the Ising-type Magnetic Anisotropy and of the Relaxation Time in Mononuclear Trigonal Bipyramidal Co(II) Single Molecule Magnets. *Inorg. Chem.* **2017**, *56* (3), 1104.

(35) Shao, F.; Cahier, B.; Guihéry, N.; Riviere, E.; Guillot, R.; Barra, A.-L.; Lan, Y.; Wernsdorfer, W.; Campbell, V. E.; Mallah, T. Tuning the Ising-type anisotropy in trigonal bipyramidal Co(ii) complexes. *Chem. Commun.* **2015**, *51* (92), 16475.

(36) Vaidya, S.; Shukla, P.; Tripathi, S.; Rivière, E.; Mallah, T.; Rajaraman, G.; Shanmugam, M. Substituted versus Naked Thiourea Ligand Containing Pseudotetrahedral Cobalt(II) Complexes: A Comparative Study on Its Magnetization Relaxation Dynamics Phenomenon. *Inorg. Chem.* **2018**, *57* (6), 3371.

(37) Vaidya, S.; Tewary, S.; Singh, S. K.; Langley, S. K.; Murray, K. S.; Lan, Y.; Wernsdorfer, W.; Rajaraman, G.; Shanmugam, M. What Controls the Sign and Magnitude of Magnetic Anisotropy in Tetrahedral Cobalt(II) Single-Ion Magnets? *Inorg. Chem.* **2016**, *55* (19), 9564.

(38) Vaidya, S.; Upadhyay, A.; Singh, S. K.; Gupta, T.; Tewary, S.; Langley, S. K.; Walsh, J. P. S.; Murray, K. S.; Rajaraman, G.; Shanmugam, M. A synthetic strategy for switching the single ion anisotropy in tetrahedral Co(II) complexes. *Chem. Commun. (Cambridge, U. K.)* **2015**, *51* (18), 3739.

(39) Sottini, S.; Poneti, G.; Ciattini, S.; Levesanos, N.; Ferentinos, E.; Krzystek, J.; Sorace, L.; Kyritsis, P. Magnetic Anisotropy of Tetrahedral CoII Single-Ion Magnets: Solid-State Effects. *Inorg. Chem.* **2016**, *55* (19), 9537.

(40) Zadrozny, J. M.; Telsler, J.; Long, J. R. Slow magnetic relaxation in the tetrahedral cobalt(II) complexes [Co(EPh)₄]₂ (EO, S, Se). *Polyhedron* **2013**, *64*, 209.

(41) Zadrozny, J. M.; Long, J. R. Slow Magnetic Relaxation at Zero Field in the Tetrahedral Complex [Co(SPh)₄]₂. *J. Am. Chem. Soc.* **2011**, *133* (51), 20732.

(42) Maganas, D.; Sottini, S.; Kyritsis, P.; Groenen, E. J. J.; Neese, F. Theoretical Analysis of the Spin Hamiltonian Parameters in Co(II)S₄ Complexes, Using Density Functional Theory and Correlated ab initio Methods. *Inorg. Chem.* **2011**, *50* (18), 8741.

(43) Suturina, E. A.; Maganas, D.; Bill, E.; Atanasov, M.; Neese, F. Magneto-Structural Correlations in a Series of Pseudotetrahedral [CoII(XR)₄]₂ Single Molecule Magnets: An ab Initio Ligand Field Study. *Inorg. Chem.* **2015**, *54* (20), 9948.

(44) Yao, Z.-S.; Wu, S.-Q.; Kitagawa, Y.; Su, S.-Q.; Huang, Y.-G.; Li, G.-L.; Ni, Z.-H.; Nojiri, H.; Shiota, Y.; Yoshizawa, K.; et al. Anisotropic Change in the Magnetic Susceptibility of a Dynamic Single Crystal of a Cobalt(II) Complex. *Angew. Chem., Int. Ed.* **2017**, *56* (3), 717.

(45) Suturina, E. A.; Nehrkorn, J.; Zadrozny, J. M.; Liu, J.; Atanasov, M.; Weyhermueller, T.; Maganas, D.; Hill, S.; Schnegg, A.; Bill, E.; et al. Magneto-Structural Correlations in Pseudotetrahedral Forms of the [Co(SPh)₄]₂ Complex Probed by Magnetometry, MCD Spectroscopy, Advanced EPR Techniques, and ab Initio Electronic Structure Calculations. *Inorg. Chem.* **2017**, *56* (5), 3102.

(46) Comba, P.; Großhauser, M.; Klingeler, R.; Koo, C.; Lan, Y.; Müller, D.; Park, J.; Powell, A.; Riley, M. J.; Wadeh, H. Magnetic Interactions in a Series of Homodinuclear Lanthanide Complexes. *Inorg. Chem.* **2015**, *54* (23), 11247.

(47) Vasiliev, A. N.; Volkova, O. S.; Zvereva, E. A.; Ovchenkov, E. A.; Munaò, I.; Clark, L.; Lightfoot, P.; Vavilova, E. L.; Kamusella, S.; Klaus, H. H.; et al. 1/3 magnetization plateau and frustrated ferrimagnetism in a sodium iron phosphite. *Phys. Rev. B: Condens. Matter Mater. Phys.* **2016**, *93* (13), 134401.

(48) Neese, F. The ORCA program system. *Wiley Interdiscip. Rev. Comput. Mol. Sci.* **2012**, *2* (1), 73.

(49) van Lenthe, E.; van der Avoird, A.; Wormer, P. E. S. Density functional calculations of molecular hyperfine interactions in the zero order regular approximation for relativistic effects. *J. Chem. Phys.* **1998**, *108* (12), 4783.

(50) van Lenthe, E.; Baerends, E. J.; Snijders, J. G. Relativistic regular two-component Hamiltonians. *J. Chem. Phys.* **1993**, *99* (6), 4597.

(51) Schaefer, A.; Horn, H.; Ahlrichs, R. Fully optimized contracted Gaussian basis sets for atoms lithium to krypton. *J. Chem. Phys.* **1992**, *97* (4), 2571.

(52) Weigend, F.; Ahlrichs, R. Balanced basis sets of split valence, triple zeta valence and quadruple zeta valence quality for H to Rn: Design and assessment of accuracy. *Phys. Chem. Chem. Phys.* **2005**, *7* (18), 3297.

(53) Ruamps, R.; Maurice, R.; Batchelor, L.; Boggio-Pasqua, M.; Guillot, R.; Barra, A. L.; Liu, J.; Bendeif, E.-E.; Pillet, S.; Hill, S.; et al. Giant Ising-Type Magnetic Anisotropy in Trigonal Bipyramidal Ni(II) Complexes: Experiment and Theory. *J. Am. Chem. Soc.* **2013**, *135* (8), 3017.

(54) Maurice, R.; Bastardis, R.; Graaf, C. d.; Suaud, N.; Mallah, T.; Guihéry, N. Universal Theoretical Approach to Extract Anisotropic Spin Hamiltonians. *J. Chem. Theory Comput.* **2009**, *5* (11), 2977.

(55) Cherkasova, T. G.; Bagryanskaya, I. Y.; Pervukhina, N. V.; Kurat'eva, N. V.; Medvedev, V. V.; Tatarinova, E. S.; Cherkasova, E. V. Hexafluorosilicates of cobalt(II) complexes with dimethylsulfoxide and dimethylformamide. *Russ. J. Inorg. Chem.* **2017**, *62* (6), 760.

(56) O'Hearn, D. J.; Singer, R. D. Direct Synthesis of a Copper(II) N-Heterocyclic Carbene Complex in Air. *Organometallics* **2017**, *36* (17), 3175.

(57) Cope, J. D.; Liyanage, N. P.; Kelley, P. J.; Denny, J. A.; Valente, E. J.; Webster, C. E.; Delcamp, J. H.; Hollis, T. K. Electrocatalytic reduction of CO₂ with CCC-NHC pincer nickel complexes. *Chem. Commun.* **2017**, *53* (68), 9442.

(58) Chen, J.-L.; Zeng, X.-H.; Luo, Y.-S.; Wang, W.-M.; He, L.-H.; Liu, S.-J.; Wen, H.-R.; Huang, S.; Liu, L.; Wong, W.-Y. Synthesis, structure, and photophysics of copper(i) triphenylphosphine complexes with functionalized 3-(2'-pyrimidinyl)-1,2,4-triazole ligands. *Dalton Trans.* **2017**, *46* (38), 13077.

(59) Kohler, L.; Hadt, R. G.; Hayes, D.; Chen, L. X.; Mulfort, K. L. Synthesis, structure, and excited state kinetics of heteroleptic Cu(i) complexes with a new sterically demanding phenanthroline ligand. *Dalton Trans.* **2017**, *46* (38), 13088.

(60) Zabrodsky, H.; Peleg, S.; Avnir, D. Continuous symmetry measures. *J. Am. Chem. Soc.* **1992**, *114* (20), 7843.

(61) The computed *E/D* value reaches the rhombic limit for complex **4** (0.33) upon inclusion of anions in the calculations. Therefore, the sign of *D* cannot be determined unambiguously. Hence, the *D_{zz}* orientation obtained from this calculation is not shown in Figure 1E.

(62) Schiessl, W.; Puchta, R.; Bugarčić, Ž. D.; Heinemann, F. W.; van Eldik, R. Systematic Counterion Tuning of the Solid-State Structure of [Pt(thiourea)₄]₂₊. *Eur. J. Inorg. Chem.* **2007**, *2007* (10), 1390.

(63) Vaidya, S.; Singh, S. K.; Shukla, P.; Ansari, K.; Rajaraman, G.; Shanmugam, M. Role of Halide Ions in the Nature of the Magnetic Anisotropy in Tetrahedral CoII Complexes. *Chem.—Eur. J.* **2017**, *23* (40), 9546.

(64) Ibrahim, M.; Lan, Y.; Bassil, B. S.; Xiang, Y.; Suchopar, A.; Powell, A. K.; Kortz, U. Hexadecacobalt(II)-Containing Polyoxometalate-Based Single-Molecule Magnet. *Angew. Chem., Int. Ed.* **2011**, *50* (20), 4708.

(65) Ishii, N.; Ishida, T.; Nogami, T. Polymorphic Alternating HNN–Cobalt(II) Chains Both Behaving as Single-Chain Magnets (HNN = 4,4,5,5-Tetramethylimidazolin-1-oxyl 3-Oxide). *Inorg. Chem.* **2006**, *45* (10), 3837.

(66) Boudalis, A. K.; Raptopoulou, C. P.; Abarca, B.; Ballesteros, R.; Chadlaoui, M.; Tuchagues, J.-P.; Terzis, A. CoII Chemistry of 2,6-Bis(2-pyridylcarbonyl)pyridine: An Icosanuclear Co Cluster Exhibiting Superparamagnetic Relaxation. *Angew. Chem., Int. Ed.* **2006**, *45* (3), 432.

(67) Banci, L.; Bencini, A.; Benelli, C.; Gatteschi, D.; Zanchini, C. *Structures versus Special Properties, Berlin, Heidelberg* **1982**, *52*, 37.

(68) Bencini, A.; Gatteschi, D. *EPR of exchange coupled systems*; Dover Publication, 2012.

(69) Stoll, S.; Schweiger, A. EasySpin, a comprehensive software package for spectral simulation and analysis in EPR. *J. Magn. Reson.* **2006**, *178* (1), 42.

(70) Maganas, D.; Milikisyants, S.; Rijnbeek, J. M. A.; Sottini, S.; Levesanos, N.; Kyritsis, P.; Groenen, E. J. J. A Multifrequency High-Field Electron Paramagnetic Resonance Study of CoII₄ Coordination. *Inorg. Chem.* **2010**, *49* (2), 595.

(71) Cucos, P.; Tuna, F.; Sorace, L.; Matei, I.; Maxim, C.; Shova, S.; Gheorghe, R.; Caneschi, A.; Hillebrand, M.; Andruh, M. Magnetic and Luminescent Binuclear Double-Stranded Helicates. *Inorg. Chem.* **2014**, *53* (14), 7738.

(72) Pilbrow, J. R. Effective g values for $S = 3/2$ and $S = 5/2$. *J. Magn. Reson. (1969-1992)* **1978**, *31* (3), 479.

(73) Krupskaya, Y.; Alfonsov, A.; Parameswaran, A.; Kataev, V.; Klingeler, R.; Steinfeld, G.; Beyer, N.; Gressenbuch, M.; Kersting, B.; Büchner, B. Interplay of magnetic exchange interactions and Ni-S-Ni bond angles in polynuclear nickel(II) complexes. *ChemPhysChem* **2010**, *11* (9), 1961.

(74) Veryazov, V.; Widmark, P.-O.; Serrano-Andres, L.; Lindh, R.; Roos, B. O. 2MOLCAS as a development platform for quantum chemistry software. *Int. J. Quantum Chem.* **2004**, *100* (4), 626.

(75) Aquilante, F.; De Vico, L.; Ferre, N.; Ghigo, G.; Malmqvist, P.-a.; Neogrady, P.; Pedersen, T. B.; Pitonak, M.; Reiher, M.; Roos, B. O.; Serrano-Andrés, L.; Urban, M.; Veryazov, V.; Lindh, R. MOLCAS 7: The Next Generation. *J. Comput. Chem.* **2010**, *31* (1), 224.

(76) Duncan, J. A. Molcas 7.2. *J. Am. Chem. Soc.* **2009**, *131* (6), 2416.

(77) Karlstroem, G.; Lindh, R.; Malmqvist, P.-A.; Roos, B. O.; Ryde, U.; Veryazov, V.; Widmark, P.-O.; Cossi, M.; Schimmelpfennig, B.; Neogrady, P.; et al. MOLCAS: a program package for computational chemistry. *Comput. Mater. Sci.* **2003**, *28* (2), 222.

(78) Chibotaru, L. F.; Ungur, L. Ab initio calculation of anisotropic magnetic properties of complexes. I. Unique definition of pseudo spin Hamiltonians and their derivation. *J. Chem. Phys.* **2012**, *137* (6), 064112.

(79) Zhurko, G. A.; Zhurko, D. A. *Chemcraft*; 2009.

(80) Ruamps, R.; Maurice, R.; Batchelor, L.; Boggio-Pasqua, M.; Guillot, R.; Barra, A. L.; Liu, J.; Bendeif, E.-E.; Pillet, S.; Hill, S.; et al. Giant Ising-Type Magnetic Anisotropy in Trigonal Bipyramidal Ni(II) Complexes: Experiment and Theory. *J. Am. Chem. Soc.* **2013**, *135* (8), 3017.